

1 **Inclusion of mountain wave-induced cooling for the**  
2 **formation of PSCs over the Antarctic Peninsula in a**  
3 **chemistry-climate model**

4  
5 **A. Orr<sup>1</sup>, J. S. Hosking<sup>1</sup>, L. Hoffmann<sup>2</sup>, J. Keeble<sup>3</sup>, S. M. Dean<sup>4</sup>, H. K. Roscoe<sup>1</sup>, N.**  
6 **L. Abraham<sup>5,3</sup>, S. Vosper<sup>6</sup>, and P. Braesicke<sup>7</sup>**

7  
8 [1]{British Antarctic Survey, NERC, Cambridge, UK}

9 [2]{Jülich Supercomputing Centre, Forschungszentrum Jülich, Jülich, Germany}

10 [3]{University of Cambridge, Cambridge, UK}

11 [4]{National Institute of Water and Atmospheric Research, Auckland, New Zealand}

12 [5]{National Centre for Atmospheric Science, University of Cambridge, Cambridge, UK}

13 [6]{Met Office, Exeter, UK}

14 [7]{Karlsruhe Institute of Technology, Karlsruhe, Germany}

15  
16 Correspondence to: A. Orr (anmcr@bas.ac.uk)

17  
18 Submitted to: *Atmospheric Chemistry and Physics*

19  
20 **Abstract**

21 An important source of polar stratospheric clouds (PSCs), which play a crucial role in  
22 controlling polar stratospheric ozone depletion, is from the temperature fluctuations induced  
23 by mountain waves. However, this formation mechanism is usually missing in chemistry-  
24 climate models because these temperature fluctuations are neither resolved nor parameterised.  
25 Here, we investigate the representation of stratospheric mountain wave-induced temperature  
26 fluctuations by the UK Met Office Unified Model (UM) at climate scale and mesoscale

1 against Atmospheric Infrared Sounder satellite observations for three case studies over the  
2 Antarctic Peninsula. At a high horizontal resolution (4 km) the regional mesoscale  
3 configuration of the UM correctly simulates the magnitude, timing, and location of the  
4 measured temperature fluctuations. By comparison, at a low horizontal resolution ( $2.5^\circ \times$   
5  $3.75^\circ$ ) the global climate configuration fails to resolve such disturbances. However, it is  
6 demonstrated that the temperature fluctuations computed by a mountain wave  
7 parameterisation scheme inserted into the climate configuration (which computes the  
8 temperature fluctuations due to unresolved mountain waves) are in relatively good agreement  
9 with the mesoscale configuration responses for two of the three case studies. The  
10 parameterisation was used to include the simulation of mountain wave-induced PSCs in the  
11 global chemistry-climate configuration of the UM. A subsequent sensitivity study  
12 demonstrated that regional PSCs increased by up to 50% during July over the Antarctic  
13 Peninsula following the inclusion of the local mountain wave-induced cooling phase.

14

## 15 **1 Introduction**

16 Gravity waves generated by stratified flow passing over orography (mountain waves) that  
17 propagate into the stratosphere can play a role in the formation of polar stratospheric clouds  
18 (PSCs). Adiabatic temperature changes resulting from mountain wave-induced vertical  
19 displacement can drive significant localised temperature fluctuations, enabling stratospheric  
20 temperatures to fall below the threshold value for PSC formation in the cold phases of these  
21 waves even if the synoptic-scale temperatures are too high. Studies of individual cases show  
22 that mountain waves formed over regions including the Antarctic Peninsula, Greenland, and  
23 northern Scandinavia are a significant source of such clouds by generating localised cooling  
24 of up to  $\sim 15$  K (e.g. Carslaw et al., 1998a; Dörnbrack et al., 1999, 2002, 2012; Noel et al.,  
25 2009).

26 The threshold temperatures for PSC formation at an altitude of around 20 km depend on  
27 composition (in particular water vapour and nitric acid) and are generally assumed to be 195  
28 K for type Ia (nitric acid trihydrate particles), 191 K for type Ib (supercooled ternary solution  
29 droplets), and 188 K for type II (water ice particles) (Pawson et al., 1995; Alfred et al., 2007).  
30 Within the centre of the Antarctic stratospheric vortex in winter, the atmosphere is so cold  
31 that temperatures are regularly below these thresholds, i.e. formation of PSCs on the synoptic-  
32 scale dominates (Campbell and Sassen, 2008). However, the synoptic-scale temperatures of

1 the edge region of the Antarctic stratospheric vortex can be warmer than the formation  
2 thresholds, and therefore not typically saturated in PSCs in winter and early spring. Hence,  
3 mountain waves can be an important source of PSCs at the edge region of the Antarctic  
4 stratospheric vortex, such as over the Antarctic Peninsula (McDonald et al., 2009; Noel and  
5 Pitts, 2012). Because of stronger planetary wave forcing, the Arctic stratospheric vortex is  
6 generally considerably warmer than that of the Antarctic. Thus, the occurrence of PSC  
7 formation temperatures on the synoptic-scale is less frequent in the Arctic (Pawson et al.,  
8 1995), thereby making mountain wave-induced PSCs an important source (Dörnbrack et al.,  
9 2001; Alexander et al., 2013). Moreover, mountain waves are a significant source of PSCs on  
10 the synoptic-scale in both the Arctic and Antarctic due to their advection far downstream of  
11 the wave event that formed them (Carslaw et al., 1999; Höpfner et al., 2006; Eckermann et al.,  
12 2009; Alexander et al., 2011).

13 The role of PSC particles in polar ozone chemistry is well understood. In the winter when  
14 there is not enough sunlight in the polar stratosphere to initiate photochemistry, the  
15 conversion of reservoir chlorine molecules into chlorine gas takes place on the surface of  
16 PSCs. In the spring when the polar stratosphere becomes sunlit, ultra-violet radiation splits  
17 the chlorine gas molecules into chlorine atoms, which take part in reactions which destroy  
18 ozone (Solomon, 1999). These reactions have resulted in the formation of the spring-time  
19 Antarctic ozone hole, which has profoundly impacted the Southern Hemisphere circulation  
20 and surface climate during summer (e.g. Orr et al., 2008, 2012; Thompson et al., 2011). With  
21 the continued implementation of the Montreal Protocol, recovery of the Antarctic ozone hole  
22 is generally anticipated by the end of the century. However, model predictions using coupled  
23 chemistry-climate simulations give a large range of estimates of the rate and timing of this  
24 recovery (Eyring et al., 2013). The fact that the results are model dependent suggests that  
25 some mechanisms are not yet fully understood. Similarly, simulations of the ozone hole  
26 covering the past few decades obtain a wide range of results, further questioning the value of  
27 these predictions (Austin et al., 2010). Accurate predictions of the timing are critical as this  
28 recovery will reshape Southern Hemisphere climate by no-longer counteracting the effects of  
29 increasing greenhouse gases (Polvani et al., 2011).

30 Therefore, to produce accurate simulations of stratospheric ozone depletion, coupled  
31 chemistry-climate models must be able to represent PSC formation mechanisms and their  
32 attendant ozone-loss chemistry due to localised dynamics such as mountain waves (Cariolle et

1 al., 1989; Carslaw et al., 1998b; Austin et al., 2010). However, current global chemistry-  
2 climate models have a horizontal resolution of some hundreds of kilometres (e.g. Morgenstern  
3 et al., 2010) at the equator and are therefore only able to explicitly resolve waves with long  
4 horizontal wavelengths (Reinecke and Durran, 2009), i.e. the temperature fluctuations  
5 associated with small-scale mountain waves are missing, leading to insufficient PSC  
6 formation in the models. Consistent with this is the systematic over-prediction of high-  
7 latitude spring time ozone increases in both hemispheres by models (Carslaw et al. 1998b,  
8 Eyring et al. 2006).

9 Mountain wave-induced stratospheric temperature fluctuations can be detected by their  
10 associated fluctuations in temperature-sensitive satellite radiance measurements from infrared  
11 scanning instruments such as the Atmospheric Infrared Sounder (AIRS) (e.g. Alexander and  
12 Barnet, 2007; Hoffmann et al., 2013). As a nadir viewing instrument, AIRS radiance  
13 measurements have a high horizontal resolution (14 km at nadir), enabling waves with short  
14 horizontal scales which are unresolved by chemistry-climate models to be visible. On the  
15 other hand, AIRS radiance measurements have a limited vertical resolution, meaning waves  
16 with short (typically  $\leq 10$  km) vertical scales are poorly resolved. Comparison between AIRS  
17 radiance measurements and model simulated radiance measurements (calculated using the  
18 simulated temperature field of the model as input for a radiative transfer model) provides an  
19 effective and direct means of validation of the model representation of gravity wave events  
20 (Grimsdell et al., 2010).

21 To improve the simulation of mountain wave-induced PSCs in a chemistry-climate model, the  
22 temperature fluctuations due to unresolved (sub-grid scale) mountain waves can be  
23 parameterised (e.g. Carslaw et al., 1999; Dean et al., 2007; Wells et al., 2011). In the  
24 parameterisation scheme of Dean et al. (2007) the mountain wave-induced temperature  
25 fluctuations were used in the cloud scheme of the HadAM3 (Hadley Centre Atmospheric  
26 Model version 3) configuration of the Met Office Unified Model (UM) to realistically  
27 represent cirrus in the upper-troposphere, which was previously under-represented over many  
28 mountain ranges.

29 In this study, the Dean et al. (2007) scheme is used to include the simulation of mountain  
30 wave-induced PSCs in the United Kingdom Chemistry and Aerosol (UKCA) module, which  
31 is the global chemistry-climate configuration of the UM (section 5). However, we only  
32 evaluate the sensitivity of PSC simulation in the chemistry-climate model to the inclusion of

1 the mountain wave-induced temperature fluctuations for one regional example, the Antarctic  
2 Peninsula. (The contribution of the scheme to global PSCs and ozone chemistry will be fully  
3 assessed in a subsequent manuscript.) This is because the main purpose of this study is to  
4 assess the ability of the parameterisation to simulate stratospheric temperature fluctuations,  
5 which is achieved by using case studies of AIRS measurements to validate high horizontal  
6 resolution simulations (using the regional mesoscale configuration of the UM) of mountain  
7 wave-induced stratospheric temperature fluctuations above the Antarctic Peninsula (section  
8 3). Following this, the Dean et al. (2007) scheme is inserted into the (low horizontal  
9 resolution) global climate configuration of the UM and its temperature fluctuations are  
10 assessed by comparing with output from the high-resolution simulations (section 4). We will  
11 demonstrate below that the high-resolution simulations are in excellent agreement with the  
12 AIRS observations, and can therefore be used as a ‘truth’ with which to investigate the  
13 performance of the parameterisation scheme.

14 The Antarctic Peninsula is chosen because strong westerly winds impinging on its high  
15 topographic ridge frequently generate large-amplitude stratospheric mountain waves  
16 (Plougonven et al., 2008; Hoffmann et al., 2013) with horizontal wavelengths of  $\sim 300$  km (as  
17 well as structures on shorter horizontal scales) and long ( $\geq 10$  km) vertical wavelengths (Wu,  
18 2004; Alexander and Teitelbaum, 2007), i.e. resolved by AIRS. The long vertical  
19 wavelengths result from wave refraction caused when the background wind speed is  
20 unidirectional and increases with height (see e.g. Wu and Eckermann, 2008). Note also that  
21 the availability of sunlight at the Peninsula during mid-winter to initiate photochemistry  
22 means that ozone depletion is substantial over this region from mid-winter onwards (Roscoe  
23 et al., 1997).

24

## 25 **2 Models, mountain wave parameterisation, data, and methodology**

### 26 **2.1 Models**

27 The UM is a numerical modelling system based on non-hydrostatic dynamics which can be  
28 run with varying configurations, including for this study as a regional mesoscale model, a  
29 global climate model, and a global chemistry-climate model. Hereafter, these models are  
30 referred to as the mesoscale, climate, and chemistry-climate models, respectively. The  
31 climate model is based on the HadGEM3 (Hadley Centre Global Environmental Model

1 version 3) configuration of the UM (Hewitt et al., 2011). The UKCA chemistry-climate  
2 model (Morgenstern et al., 2009) runs within the UM climate configuration. UKCA uses a  
3 simplified scheme for forming and evaporating PSCs, based on the assumption that the gas  
4 and condensed phase of  $\text{HNO}_3$  are in equilibrium (Morgenstern et al., 2009). Here, both the  
5 climate and chemistry-climate configurations are atmosphere-only models based on version  
6 7.3 of the UM, with a horizontal resolution of N48 ( $96 \times 73$  grid points, or  $2.5^\circ \times 3.75^\circ$ ) and  
7 60 vertical levels (going up to 84 km). Version 7.3 of the UM was selected for the global  
8 modelling exercise because of its current use in a recent, comprehensive model inter-  
9 comparison (SPARC, 2013).

10 The mesoscale model is based on version 7.6 of the UM, and is similar to that described in  
11 Orr et al. (2014). It is atmosphere-only with a model domain centered over the Antarctic  
12 Peninsula, comprising  $388 \times 460$  grid points with a horizontal resolution of 4 km and 85  
13 vertical levels (reaching up to 85 km). Following Webster et al. (2008), it uses the option of a  
14 fully three-dimensional potential temperature advection scheme, in conjunction with reduced  
15 temporal off-centering, to better represent resolved gravity waves. Orography is interpolated  
16 from a high-resolution digital elevation model of Antarctica (version 9 of the Radarsat  
17 Antarctic Mapping Project, Liu et al. 2001). The mesoscale model is nested within a global  
18 version of the model with a horizontal resolution of N512 ( $1024 \times 769$  grid points, or  $0.352^\circ$   
19  $\times 0.234^\circ$ ) and 70 vertical levels (reaching up to 80 km) that is used (following a 3 h spin-up)  
20 to initiate and provide boundary conditions for the simulation. Note that initialisation values  
21 for sea ice state and sea surface temperature for the mesoscale model were obtained from  
22 high-resolution ( $\sim 5$  km scale) daily Operational Sea Surface Temperature and Sea Ice  
23 Analysis (OSTIA) data (Donlon et al. 2011). The Met Office operational analysis is used to  
24 initialise the global model. Version 7.6 of the UM was selected for the mesoscale model as it  
25 included improvements which reduced the occurrence of spurious cooling in partially  
26 resolved valleys.

27 Note that all of the configurations of the UM parameterise the vertical divergence of mountain  
28 wave-induced momentum flux (i.e. orographic gravity wave drag), which influences the  
29 atmospheric circulation. This is dealt with by the orographic gravity wave drag scheme of  
30 Webster et al. (2003), which should not be confused with the mountain wave-induced  
31 temperature fluctuation scheme of Dean et al. (2007), described below.

## 1 2.2 Description of the mountain wave parameterisation

2 By assuming that waves are forced by steady flow over a two-dimensional ridge and that  
3 vertical variations of the background atmospheric state are slowly varying (compared to the  
4 wave phase), the scheme described by Dean et al. (2007) derives generalised expressions for  
5 the maximum and minimum vertical streamline displacement (resulting in cooling and  
6 warming, respectively) associated with gravity waves induced by sub-grid scale orography  
7 (SSO). These expressions are used to compute the maximum negative  $\Delta T_{SSO}^-$  and positive  
8  $\Delta T_{SSO}^+$  temperature fluctuations associated with the displacement, which are derived using the  
9 local potential temperature gradient (Wells et al., 2011). The overall temperature fluctuation  
10 induced is subsequently calculated as  $\Delta T_{SSO} = \Delta T_{SSO}^+ + \Delta T_{SSO}^-$ . Waves are launched at every  
11 model grid box over land and at every model time step.

12 The expressions for the maximum and minimum streamline displacement depend on both the  
13 wave phase and peak vertical streamline displacement amplitude (hereafter referred to as  
14 wave amplitude), which are determined as follows. The vertical propagation is based on  
15 linear theory for hydrostatic waves forced by steady, stably stratified flow over a two-  
16 dimensional ridge, assuming that vertical variations of the background atmospheric state are  
17 slowly varying. McFarlane (1987) showed that under these circumstances and in the absence  
18 of dissipation mechanisms that the vertical evolution of the wave amplitude is determined by  
19 the decrease in density of the atmosphere with height and by changes in the horizontal wind  
20 speed  $U$  (resolved in the direction of the wave vector) and the Brunt-Väisälä frequency  $N$ .  
21 Dissipation mechanisms such as wave-breaking and critical level absorption are introduced by  
22 preventing the amplitude from exceeding the local “saturation amplitude” for which the wave  
23 field becomes unstable ( $= U / NF_{sat}$ , where  $F_{sat}$  is the critical Froude number for saturation).  
24 The vertical evolution of the wave phase is determined by changes in  $U$  and  $N$ , i.e. the Scorer  
25 parameter  $l(\approx N / U)$ .

26 To complete the determination of the wave phase and amplitude, their initial values at the top  
27 of the blocked layer must be decided. The initial wave phase is set equal to zero. The initial  
28 wave amplitude is set equal to the “effective” mountain height  $h_{eff}$  ( $= h - h_b$ , where  $h$  is the  
29 height of the sub-grid scale mountain and  $h_b$  is the height of the blocked layer that occurs at  
30 low Froude number), i.e. the maximum vertical displacement of streamlines able to pass over  
31 the top of the mountain. This is strongly dependent on the direction of the low-level wind

1 relative to the principle axis of the SSO (which preferentially aligns as ridges), and ensures  
2 that the surface amplitude is large (small) when the wind is perpendicular (parallel) to a ridge.  
3 Here,  $h = n_\sigma \sigma$ , where  $\sigma$  is the standard deviation of the SSO height from the grid-box mean  
4 and  $n_\sigma$  is a constant (such that  $n_\sigma \sigma$  approximates the physical envelope of the peaks), and  
5  $h_b = h - U_0 / N_0 F_c$ , where  $F_c$  is the critical Froude number at which flow blocking is deemed  
6 to first occur, and the subscript “0” refers to the surface layer, represented by averaging  $U$  and  
7  $N$  between the surface and  $h$ . Note that to implement the directional dependence of the  
8 surface amplitude,  $U_0$  is resolved in the direction perpendicular to the principle axis of the  
9 sub-grid orography (i.e. the direction of the wave vector). This differs from the  
10 implementation in Dean et al. (2007) which represents the directional dependence by defining  
11 the standard deviation  $\sigma$  of the SSO height in the surface wind direction.

12 The parameterisation scheme is (globally) implemented in the climate and chemistry-climate  
13 configurations of the UM. The SSO parameters used by the scheme are based on Lott and  
14 Miller (1997). In the scheme the parameters  $n_\sigma$ ,  $F_{sat}$  and  $F_c$  are treated as tuneable.  
15 Following an initial sensitivity study (specific to the Antarctic Peninsula, not shown) to  
16 optimise the performance of the scheme, their values were set to  $n_\sigma = 3$ ,  $F_{sat} = 2$  and  $F_c = 4$ .

### 17 **2.3 Data**

18 AIRS (Aumann et al., 2003) is aboard the National Aeronautics and Space Administration's  
19 Aqua satellite, which was launched in May 2002. AIRS measures the thermal emissions of  
20 atmospheric constituents in the nadir and sub-limb observation geometry. An across-track  
21 scan consists of 90 individual footprints and covers a distance of 1765 km on the ground. The  
22 along-track distance between two scans is 18 km. The AIRS aperture is  $1.1^\circ$ , corresponding to  
23 a horizontal resolution of 13.5 km at nadir and  $41 \text{ km} \times 21.4 \text{ km}$  at the scan extremes. The  
24 AIRS radiance measurements cover wavelength ranges from 3.74 to  $15.4 \mu\text{m}$  with a total of  
25 2378 radiance channels. The absolute error of the radiometric calibration is less than 0.2 %.  
26 The noise equivalent delta temperature is about 0.39 K at 250 K scene temperature for the  
27 spectral channel ( $666.5 \text{ cm}^{-1}$ ) considered here. The analyses presented in this paper are based  
28 on consolidated version 5 data products made freely available by NASA. The equatorial  
29 crossing of Aqua occurs at 13:30 LT (ascending orbit) and 01:30 LT (descending orbit). At  
30 high latitudes there is a quick transition between day- and night-time observations (e.g.,  
31 Hoffmann et al., 2013). The Antarctic Peninsula is typically covered by four satellite



1 overpasses per day. A more detailed description of AIRS is given in e.g. Hoffmann and  
2 Alexander (2009, 2010); Grimsdell et al. (2010); or Hoffmann et al. (2013).

3 Infrared radiance measurements in the 4.3 and 15  $\mu\text{m}$   $\text{CO}_2$  bands are of particular interest for  
4 the study of stratospheric gravity waves. These bands get optically thick in the stratosphere  
5 and as the  $\text{CO}_2$  concentration does not vary substantially in the lower and middle atmosphere,  
6 the radiance measurements in these channels are most sensitive to atmospheric temperature.  
7 Hoffmann and Alexander (2009) show the temperature kernel functions for the individual  
8 AIRS channels covering the 4.3 and 15  $\mu\text{m}$   $\text{CO}_2$  bands. In this study we selected the 666.5  
9  $\text{cm}^{-1}$  radiance channel of AIRS, which is within the 15  $\mu\text{m}$   $\text{CO}_2$  band. The temperature  
10 weighting function of this channel is given in Fig. 1, which shows that the brightness  
11 temperatures BT are most sensitive to atmospheric temperature at an altitude of 22 km, with  
12 full width at half maximum of 9 km. The altitude range covered by the 666.5  $\text{cm}^{-1}$  channel is  
13 of particular interest for the formation of PSCs. As the kernel function drops to less than 1 %  
14 of maximum sensitivity below 14 km, there is little interference from tropospheric emissions  
15 from clouds or water vapour.

## 16 **2.4 Methodology**

17 Three instances of stratospheric mountain waves observed over the Antarctic Peninsula by  
18 AIRS, characterised by large amplitude and long vertical wavelength, occurred on 7 August  
19 2011 at 03:40 UTC (case study 1, hereafter CS1), 2 August 2010 at 18:59 UTC (case study 2,  
20 hereafter CS2), and 14 July 2010 at 20:00 UTC (case study 3, hereafter CS3). These events  
21 were simulated by running the mesoscale model nested within a global model version of the  
22 model initialised on 5 August 2011 at 12:00 UTC for CS1, 1 August 2010 at 00:00 UTC for  
23 CS2, and 13 July 2010 at 00:00 UTC for CS3. The mesoscale model output times  
24 (integration time) closest to the actual measurement time are at 03:00 UTC on 7 August 2011  
25 (T + 39 h) for CS1, at 19:00 UTC on 2 August 2010 (T + 43 h) for CS2, and at 20:00 UTC on  
26 14 July 2010 (T + 44 h) for CS3 (note that for simplicity the mesoscale model integration  
27 times are given relative to the time of the global model initialisation). The output times  
28 reflect that the simulation of the mountain wave field requires at least a 24 h spin-up  
29 (Plougonven et al., 2010). Table 1 summarises this information. Figure 2 shows the near-  
30 surface (850 hPa) wind field simulated by the mesoscale model at the output time for each  
31 case study, showing that each of the mountain wave events were coincident with strong

1 westerly or north-westerly winds incident to the Peninsula. These winds showed the requisite  
2 strengthening with height required for the mountain waves to have long vertical wavelengths  
3 which were visible to AIRS (not shown).

4 To verify the mesoscale model simulations, the Juelich Rapid Spectral Simulation Code  
5 (JURASSIC) radiative transfer model (Hoffmann and Alexander, 2009) was used to compute  
6 model simulated AIRS radiances at  $666.5 \text{ cm}^{-1}$ . For comparison, both the real and mesoscale  
7 model simulated AIRS radiances are subsequently converted into their corresponding BT  
8 values. Brightness temperature perturbations  $\Delta BT$  were computed by removing a background  
9 brightness temperature, which was determined by fitting a 4th-order polynomial (e.g. Wu,  
10 2004; Alexander and Barnet, 2007; Hoffmann and Alexander, 2010). This fit removes slowly  
11 varying atmospheric signals, e.g. from planetary waves and general scan-angle dependence of  
12 radiances due to the sub-limb geometry. For the AIRS measured radiances the fit was carried  
13 out for each scan in the across-track direction; for the mesoscale model simulated radiances it  
14 was carried out for each latitudinal band of the model grid. In both cases it was found that the  
15 fits are well constrained by the data and the process did not introduce any artificial wave-like  
16 structures that could obfuscate the results. In order to avoid the suppression of waves with  
17 fronts parallel to the fit direction the AIRS measured (simulated) background estimates were  
18 smoothed by a 300 km running mean in the along-track (longitudinal) direction. Finally,  
19 mesoscale model estimates of  $\Delta BT$  are re-gridded to the AIRS measurement grid.

20 The mesoscale model simulations of the three case studies were repeated using the climate  
21 model (i.e. the climate model is initialised using the same Met Office operational analysis and  
22 integrated forward in time for 48 h). Comparison of the mesoscale model and climate model  
23 simulations of the near-surface winds at the time of the mountain wave events (Fig. 2) shows  
24 relatively small differences in the large-scale flow impacting the Peninsula, i.e. the large-scale  
25 atmospheric conditions responsible for the initial forcing of the mountain waves are broadly  
26 similar in both models. As the mountain wave parameterisation scheme is implemented in the  
27 climate model, the temperature fluctuations over the Antarctic Peninsula predicted by the  
28 scheme  $\Delta T_{SSO}$ , as well as the temperature fluctuations explicitly resolved by the climate  
29 model  $\Delta T_{CLIM}$  (computed by removing the background temperature, determined by fitting a  
30 4th-order polynomial), can be assessed by comparing with those from the mesoscale model.  
31 Using the mesoscale model simulations enables investigation of the vertical profile of the  
32 parameterised output, in particular the vertical evolution of the wave phase, which is not

1 possible at good vertical resolution using AIRS data alone. In the climate model  
2 implementation,  $\Delta T_{SSO}$  is passed solely to the model output to enable its evaluation and is not  
3 used by the dynamical core or any other parameterisation scheme.

4 Finally, to assess the sensitivity of the PSC scheme used by the UKCA chemistry module to  
5 the mountain wave parameterisation, perturbation and control experiments using the  
6 chemistry-climate model were conducted. The equilibrium PSC scheme provides a realistic  
7 representation of the existence of PSC particles when air temperatures drop below the PSC  
8 temperature formation threshold (e.g. Feng et al., 2011). However, the scheme does not  
9 represent a slow decline of PSC existence when temperatures rise abruptly above the  
10 temperature threshold. Instead PSCs cease to exist instantaneously in the scheme. For this  
11 reason only the cooling phase  $\Delta T_{SSO}^-$  of the parameterised temperature fluctuations are  
12 coupled to the PSC scheme as the net impact on additional PSC formation will be more  
13 realistic. Consequently the warm phase is neglected and the net effect on PSC existence might  
14 be slightly overestimated. Carslaw et al. (1999) argue that this approach is also physically  
15 justified as the warming phase of the wave-induced temperature fluctuations is typically of  
16 short enough duration that the complete evaporation of the PSC particles is unlikely to occur  
17 before temperatures fall again. In addition, evaporation will not occur if the synoptic-scale  
18 temperatures are sufficiently low that the warming phase still results in the temperature being  
19 below the PSC threshold value. In the perturbation experiments the mountain wave  
20 parameterisation is switched on. The PSC scheme computes a “total” temperature, used only  
21 by itself, by combining the temperature explicitly resolved by the chemistry-climate model  
22  $T_{CHEM-CLIM}$  with  $\Delta T_{SSO}^-$ . In the control experiment the mountain wave scheme is switched off.  
23 Both the perturbation and control experiments were run for 30 years (following a 30 year  
24 spin-up period) for a perpetual year-2000, using prescribed sea-surface temperature and sea  
25 ice fraction. For this part of the study we again concentrate on results for the Antarctic  
26 Peninsula, focusing on the month of July.

27

### 28 **3 Mesoscale model verification**

29 Figure 3 compares maps of measured and mesoscale model simulated estimates of  $\Delta BT$  for  
30 each of the three case studies. In the left panels the measured field  $\Delta BT_{AIRS}$  shows warm and  
31 cold temperature disturbances of amplitude 2-3 K clearly aligned with the western side of the

1 Peninsula mountain ridge, i.e. typical of phase fronts associated with a mountain wave caused  
2 by low-level westerly flow passing over the Peninsula and propagating upward in the  
3 atmosphere. In the right panels the amplitude and structure of the corresponding mesoscale  
4 model field  $\Delta BT_{MES}$  agrees well with the measurements.

5 Figure 4 compares  $\Delta BT_{AIRS}$  and  $\Delta BT_{MES}$  in more detail by examining their variation along the  
6 west-east orientated lines displayed in Fig. 3. The mountain wave appears prominently in  
7 both fields, with the mesoscale model producing a similar looking temperature disturbance to  
8 that measured. There are slight differences in terms of the wave amplitude, e.g. the mesoscale  
9 model amplitude in CS3 is slightly larger than that measured.

10 Note that in addition to a coherent mountain wave structure, Figs. 3 and 4 also show highly  
11 localised temperature fluctuations. For AIRS these fluctuations are partly due to increasing  
12 instrumental noise with low scene temperatures. The nominal noise of 0.39 K at 250 K scene  
13 temperature scales to 0.67 – 0.78 K at 190 – 200 K, which is more representative for the  
14 situations observed here.

15

#### 16 **4 Assessment of the mountain wave parameterisation**

17 Having shown a very good comparison between measured and mesoscale model simulated  
18  $\Delta BT$  over the Antarctic Peninsula, we can now use the temperature fluctuations simulated by  
19 the mesoscale model  $\Delta T_{MES}$  to assess the parameterised temperature fluctuations  $\Delta T_{SSO}$ , as  
20 well as the temperature fluctuations explicitly resolved by the climate model  $\Delta T_{CLIM}$ . Due to  
21 the occurrence of spatially highly localised and strongly varying temperature fluctuations, the  
22 fairest approach is to compare profiles of  $\Delta T_{SSO}$  and  $\Delta T_{CLIM}$  for a particular ( $2.5^\circ \times 3.75^\circ$ )  
23 climate model grid box with the mean and spread ( $\pm$  two standard deviations) of  $\Delta T_{MES}$  for all  
24 the mesoscale model points within the same ( $2.5^\circ \times 3.75^\circ$ ) climate model grid box. The  
25 representative climate model grid boxes for each of the three case studies are selected to  
26 coincide with the location of their respective mountain wave events. Using Fig. 3 for  
27 guidance, the grid boxes are located at ( $70^\circ\text{S}, 63.75^\circ\text{W}$ ) for CS1, ( $65.0^\circ\text{S}, 60.0^\circ\text{W}$ ) for CS2,  
28 and ( $70.0^\circ\text{S}, 60^\circ\text{W}$ ) for CS3 (these locations are also shown on Fig. 3). The comparison in  
29 Fig. 5 shows that for two of the case studies (CS1 and CS3) that  $\Delta T_{SSO}$  and the mean  $\Delta T_{MES}$   
30 response are in relatively good agreement in terms of amplitude (which ranges from 0 to 10 K

1 in the lower stratosphere), while  $\Delta T_{SSO}$  and the mean  $\Delta T_{MES}$  response are slightly out of  
2 alignment in terms of phase, evident by the maximum and minimum values of  $\Delta T_{SSO}$  differing  
3 by roughly 1 km from the mean  $\Delta T_{MES}$  response. However, at all altitudes  $\Delta T_{SSO}$  lies within  
4 the spread of  $\Delta T_{MES}$  (which in CS3 exceeds  $\pm 15$  K in the lower stratosphere), suggesting that  
5 the parameterised temperature fluctuations are representative of the range of mesoscale model  
6 responses. By contrast, in CS2 the agreement between  $\Delta T_{SSO}$  and the mean  $\Delta T_{MES}$  response is  
7 poor, marked by the failure of the parameterised response to suggest any temperature  
8 fluctuation whatsoever. However, inspection of Fig. 2 suggests that the reason for this  
9 reduced performance could be because the surface winds in CS2 are significantly  
10 underestimated in the climate model compared to the mesoscale model, which would result in  
11 a significantly weaker parameterised response than in reality. (Poorer skill in the climate  
12 model representation of surface winds would be expected due to its poorly described resolved  
13 orography.) Finally, the comparison also shows that for all three case studies that  
14  $\Delta T_{CLIM}$  completely fails to represent any temperature fluctuations, i.e. confirmation that the  
15 horizontal scale of the mountain waves are too small to be resolved by climate models, and  
16 hence their effects must be parameterised. Note that the climate model simulations of the  
17 three case studies were repeated at a higher N96 resolution ( $192 \times 145$  grid points, or  $1.875^\circ \times$   
18  $1.25^\circ$ ), which also completely failed to resolve any temperature fluctuations over the  
19 Peninsula (not shown).

20 Figure 6 (a, b) compares  $\Delta T_{MES}$  and  $\Delta T_{SSO}$  for CS3 along a west-east cross section intersecting  
21 the Peninsula at  $70^\circ\text{S}$ , i.e. again selected to coincide with the location of its mountain wave  
22 event. Only results for CS3 are shown as equivalent results for CS1 were largely similar.  
23 The predominant feature of the  $\Delta T_{MES}$  response is, as expected, a large-amplitude, vertically  
24 propagating mountain wave with phase lines tilting upstream with height, characterised by a  
25 horizontal wavelength of around 200 km, a vertical wavelength of around 15 km, and a  
26 amplitude of up to 15 K (in the lower stratosphere). It is clearly apparent that although the  
27 parameterisation scheme qualitatively captures the mesoscale model estimate of the  
28 temperature fluctuations in the lower stratosphere directly above the Peninsula, it: (i) fails to  
29 capture the upstream tilt of the phase lines, i.e. its phase lines are horizontal and do not tilt  
30 with height, and (ii) significantly underestimates the amplitude of the temperature  
31 fluctuations. (Note that Fig. 6 also demonstrates that the approach used in Fig. 5 to assess the

1 parameterised temperature fluctuations is a much more quantitative comparison than simply  
2 averaging over a long transect intersecting the Peninsula, as the negative (cooling) and  
3 positive (warming) phases apparent in Fig. 6 (a) would largely cancel each other out.)  
4 The lack of phase tilt is due to the parameterised wave field being represented by a  
5 hydrostatic gravity wave launched from an isolated bell-shaped ridge for each grid-box,  
6 which is then only propagated vertically through the column of air above. This simplification  
7 is also prohibitive in modelling the full downstream response. At climate model resolution the  
8 Antarctic Peninsula is multiple grid boxes wide as its resolved orography field is hugely  
9 smoothed/flattened (see Fig. 6) and is thus represented in the parameterisation as a series of  
10 very similar sub-grid ridges, while in the mesoscale model the Peninsula is resolved as a  
11 dominant wide single ridge. Therefore the parameterisation produces a simplified broad  
12 response, which has smaller amplitude compared to the mesoscale model, across the  
13 Peninsula, whereby any change in phase can only result from changes in  $U$  and  $N$  within each  
14 vertical column across the Peninsula. Further comparison of the mesoscale model and climate  
15 model simulations in Figs 7 and 8 shows, with the exception of the lower altitude parts of CS1  
16 and CS3, that  $U$  and  $N$  simulated by the climate model lie within the spread of the mesoscale  
17 model responses, i.e. indicating that the large-scale atmospheric conditions responsible for the  
18 parameterised phase evolution are representative of the range of mesoscale model responses.  
19 Furthermore, given its broad-scale response, it cannot be expected that the parameterised  
20 temperature fluctuations match the amplitude of the fine-scale fluctuations simulated by the  
21 mesoscale model.

22

## 23 **5 Impact of the mountain wave parameterisation on PSC formation**

24 Having shown that the parameterised mountain wave-induced temperature fluctuations are  
25 broadly consistent with the mesoscale model results, we can progress to assessing the impact  
26 of including the wave-induced cooling phase  $\Delta T_{SSO}^-$  in the chemistry-climate model and  
27 coupling it to the PSC scheme, again concentrating on the Antarctic Peninsula. Figure 6 (c)  
28 demonstrates the cooling phase  $\Delta T_{SSO}^-$  for CS3. It is apparent that in this instance it reaches  
29 values of around -10 K, which is significantly colder than the cold phases of the overall  
30 parameterised temperature fluctuations shown in Fig. 6 (b). In the first instance, we will  
31 examine the impact on the temperatures seen by the PSC scheme. Figure 9 shows for July at

1 a height of 21 km the 30-year average difference in the frequency  $f$  of the temperature  
 2 falling below the 195 K and 188 K thresholds for PSC formation of type Ia and II,  
 3 respectively. The differences are between the frequency based on the explicitly resolved  
 4 temperature  $T_{CHEM-CLIM}$  plus  $\Delta T_{SSO}^-$  from the perturbation run, and the frequency based solely  
 5 on the explicitly resolved temperature of the perturbation run, i.e.  $f_{T_{CHEM-CLIM} + \Delta T_{SSO}^-} - f_{T_{CHEM-CLIM}}$ .  
 6 The differences in frequency are always positive, which is consistent with only mountain  
 7 wave cooling being used. The results show that over much of the Peninsula, the impact of the  
 8 mountain wave cooling is to increase the frequency that the 195 K threshold is exceeded,  
 9 peaking over its northern tip with a frequency difference of 4 percentage points. By  
 10 comparison, the impact on the 188 K temperature threshold is even more dramatic, resulting  
 11 in differences which are both larger and extending much further south, peaking over  
 12 Alexander Island to the south-west of the Peninsula with a frequency difference of over 6  
 13 percentage points. The fact that the differences in 195 K threshold frequency are located  
 14 predominately over the middle and northern sections of the Peninsula is consistent with the  
 15 climatological 195 K isotherm of the perturbation run being situated at approximately  $-75^\circ$   
 16 latitude (not shown). Hence, any increase in the frequency of temperatures falling below 195  
 17 K as a result of the parameterisation can only occur northward of this, i.e. where the large-  
 18 scale temperature is not already less than 195 K. Similarly, the differences in 188 K threshold  
 19 frequency which encompass the entire length of the Peninsula are consistent with the model  
 20 188 K isotherm being situated southward of the 195 K isotherm (not shown). Figure 10  
 21 compares the 30-year temperature distribution based on  $T_{CHEM-CLIM} + \Delta T_{SSO}^-$  of the  
 22 perturbation run against that of  $T_{CHEM-CLIM}$  for the perturbation run for the same N48 grid box  
 23 used for Figs. 5, 7 and 8, again for July and at 21 km. As expected, inclusion of the  
 24 parameterised mountain wave cooling shifts the temperature distribution to lower  
 25 temperatures. In particular, it causes a longer left tail of the temperature distribution which  
 26 extends down to 177 K (or 5 K colder than the temperature distribution based solely on  
 27  $T_{CHEM-CLIM}$ ).

28 The effect of the parameterisation on PSCs is investigated by evaluating the 30-year average  
 29 difference in PSC surface area density between the perturbation and control simulations  
 30 (perturbation minus control). PSC surface area density controls the amount of reactive  
 31 chlorine species produced, which cause ozone destruction. Figure 11 shows the difference in

1 PSC surface area density at a height of 21 km for July. The perturbation run results in  
2 increases in surface area density for all PSCs (i.e. combined type I and II) of  $6\text{-}10\ \mu\text{m}^2\ \text{cm}^{-3}$   
3 over the Antarctic Peninsula and  $>10\ \mu\text{m}^2\ \text{cm}^{-3}$  over the Bellingshausen Sea. Relative to the  
4 control run, these are equivalent to increases of more than 50% over the northern tip of the  
5 Antarctic Peninsula, and at least 30% over the Bellingshausen Sea. The Weddell Sea region  
6 shows a non-significant decrease in PSC surface area density. What is of note here is that  
7 PSC differences are occurring both upstream and downstream of the Antarctic Peninsula, i.e.  
8 removed from the actual region where the parameterisation acts directly. This is not  
9 unexpected. The chemistry-climate model is interactive: Changing PSCs change chlorine  
10 activation, which impacts ozone loss. Changing ozone alters the heating rates that impact  
11 temperatures and circulation. What is diagnosed in Fig. 11 (and related figures) is the  
12 difference between two climate equilibrium states for identical boundary conditions (compare  
13 e.g. Braesicke et al., 2013). Consequently, what is shown in the figures is locally strongly  
14 influenced by the additional parameterisation (adding localised cooling and thus producing  
15 more PSCs), but in regions away from the direct impact the response can be determined by  
16 feedback mechanisms. Figure 11 additionally separates these differences into their individual  
17 contributions from type I and type II PSCs. It is type I (type II) PSCs which are largely  
18 responsible for the overall PSC increase over the Antarctic Peninsula (Bellingshausen Sea).

19

## 20 **6 Summary and discussion**

21

22 Based on three case studies, this study demonstrated that: (i) UM high-resolution (4 km)  
23 mesoscale model simulations are able to accurately simulate the large mountain wave-induced  
24 temperature fluctuations in the lower stratosphere associated with strong westerly or north-  
25 westerly flow over the Antarctic Peninsula, and (ii) UM low-resolution ( $2.5^\circ \times 3.75^\circ$ ) climate  
26 model simulations are completely unable to resolve such temperature fluctuations. These  
27 fluctuations act as a significant source of localised PSC formation as they enable stratospheric  
28 temperatures which otherwise would remain above the temperature threshold for PSC  
29 formation, to fall below it. With low-resolution a model is unable to resolve such temperature  
30 fluctuations, and as a consequence would underestimate mountain wave-induced PSCs and  
31 the attendant PSC-induced ozone depletion.



1 To investigate the parameterisation of temperature fluctuations due to unresolved (sub-grid  
2 scale) mountain waves, the parameterisation of Dean et al. (2007) was implemented in the  
3 UM climate model. It describes the vertical evolution of a linear hydrostatic wave forced by  
4 steady, stably stratified flow over a two-dimensional ridge. By determining the vertical  
5 evolution of the wave amplitude and the wave phase (alternative schemes such as Wells et al.  
6 (2011) solely compute the wave amplitude), the parameterisation is able to calculate the  
7 maximum downward and upward vertical displacement and subsequently the associated  
8 positive and negative temperature fluctuations. Its ability to represent the temperature  
9 fluctuations associated with the three case studies was assessed by comparison with the  
10 mesoscale model response. This demonstrated that for two out of the three case studies that:  
11 (i) the parameterised temperature fluctuations lie within the spread of the mesoscale model  
12 response, and (ii) the amplitude and phase of the parameterised temperature fluctuations are  
13 broadly in agreement with the mean mesoscale model response. In the remaining case study  
14 the parameterised response failed to capture any temperature fluctuations whatsoever, which  
15 we suggest is due to poor skill in capturing surface winds by the climate model. However, the  
16 comparison also showed that the parameterisation cannot represent the upstream tilt of the  
17 phase lines with height. This is due to it representing the Peninsula by a series of independent  
18 sub-grid scale ridges which each launch a mountain wave vertically through the column of air  
19 above. Moreover, the parameterisation also does not represent trapped mountain lee waves,  
20 which can result in localised cooling (and the formation of PSCs) many hundreds of  
21 kilometres downstream (e.g. Dörnbrack et al., 1999). Notwithstanding these deficiencies, the  
22 current study illustrates that a more comprehensive treatment of sub-grid scale mountain  
23 waves in a global climate model leads to realistic localised temperature change diagnostics.

24 Subsequently, we assessed and characterised the localised impact of the parameterised  
25 temperature fluctuations in a comprehensive chemistry-climate model. The formation of  
26 PSCs is dependent on the temperature being below a threshold value, and the argument that  
27 the warm phase is too short to lead to particle evaporation (Carslaw et al., 1999) means that  
28 the presence of PSCs is more strongly controlled by the cooling phase. It was found that  
29 adding the wave-induced cooling phase to the resolved temperature had a substantial impact  
30 on the frequency and magnitude of low temperatures which satisfy PSC thresholds, resulting  
31 in a regional 30-50 % increase in PSC surface area density during July at a height of 21 km  
32 over the Antarctic Peninsula and the Bellingshausen Sea. It should be stressed that we were  
33 unable to compare these results with observations as: (i) detailed measurements of Antarctic

1 PSCs over a decadal time scale are not available at present (Austin et al., 2010), and (ii)  
2 global atmospheric reanalyses do not resolve small-scale temperature fluctuations.

3 Our decision to include only the cooling phase implies that this may lead to an overestimate  
4 of the impacts of the scheme, and that the diagnosed increase in PSC surface area density  
5 should perhaps be considered as an upper bound. Note that consideration of the (neglected)  
6 warm phase in the equilibrium PSC scheme would reduce the PSC surface area density  
7 change modelled towards the large scale solution obtained in the control integration. By  
8 contrast, in a microphysical scheme in which PSC particles are advected around, the particles  
9 could briefly exist in air which is above the threshold temperature during the wave-induced  
10 warming phase before temperature will fall once again to below the threshold, maintaining  
11 PSCs. We simulate this effect by using the cooling phase only. In future work we plan is to  
12 insert the microphysical scheme DLAPSE (Denitrification by Lagrangian Particle  
13 Sedimentation) (Feng et al., 2011) into the UKCA module, and couple it to both the cooling  
14 and warming phases of the parameterised temperature fluctuations.

15 The simulation of PSC differences both upstream and downstream of the Antarctic Peninsula,  
16 and hence removed from the actual region where the parameterisation impacts temperatures  
17 directly, is suggestive of a new climate-equilibrium state being established in the model that  
18 allows non-local effects to occur. Investigation of this will be the subject of future study.  
19 Nevertheless, the parameterisation offers a method for improving lower stratospheric  
20 temperatures that more often satisfy conditions for PSC formation, the failure of which was  
21 suggested by Austin et al. (2010) to be one of the main reasons for the poor simulation of  
22 ozone depletion.

23 It is worth noting that other biases can affect the ability of chemistry-climate models to  
24 realistically simulate PSCs. For example, the failure of many models to represent the effects  
25 of non-orographic gravity wave drag can result in unrealistically cold temperatures in the  
26 Southern Hemisphere winter stratosphere (Orr et al., 2010), i.e. resulting in synoptic-scale  
27 temperatures which fall below the PSC temperature threshold when in reality they should be  
28 above it, which as a consequence cause the formation of too many PSCs and associated  
29 increased ozone losses (Austin et al., 2003). Moreover, the equilibrium PSC scheme used by  
30 the UKCA module does not advect PSC particles (Feng et al., 2011). This means that the  
31 occurrence of circumpolar belts of PSCs which have been attributed to mountain wave-  
32 induced PSCs over regions such as the Antarctic Peninsula would not be represented.

1 However, DLAPSE uses a Lagrangian trajectory scheme and as such is able to transport PSC  
2 particles away from the region of formation (Feng et al., 2011). Further future work will also  
3 involve evaluating and improving the representation of PSC formation mechanisms in the  
4 chemistry-climate model via comparison with MIPAS (Michelson Interferometer for Passive  
5 Atmospheric Sounding) PSC observations (Spang et al., 2012), resulting in improved  
6 modelling and more reliable projections of both Antarctic ozone hole recovery and Arctic  
7 ozone.

8

## 9 **Acknowledgements**

10 The authors thank the two anonymous reviewers for their remarks which contributed to the  
11 improvement of the original manuscript. Thanks are also given to T. Phillips for providing  
12 much assistance in producing the figures, and to S. Webster, T. Lachlan-Cope, C. Listowski,  
13 K. Carslaw and G. Mann for useful discussions. This study is part of the British Antarctic  
14 Survey Polar Science for Planet Earth Programme. It was funded by The Natural Environment  
15 Research Council (grant number NE/H022988/1). AIRS data are distributed by NASA  
16 Goddard Earth Science Data Information and Services Center. This work made use of the  
17 facilities HECToR, the UK's national high-performance computing service, which is provided  
18 by UoE HPCx Ltd at the University of Edinburgh, Cray Inc and NAG Ltd, and funded by the  
19 Office of Science and Technology through EPSRC's High End Computing Programme.

20

## 21 **References**

22 Alfred, J., Fromm, M., Bevilacqua, R., Nedoluha, G., Strawa, A., Poole, L., and Wickert, J.:  
23 Observation and analysis of polar stratospheric clouds detected by POAM III and SAGE III  
24 during the SOLVE II/VINTERSOL campaign in the 2002/2003 Northern Hemisphere winter,  
25 *Atmos. Chem. Phys.*, 7, 2151-2163, doi:10.5194/acp-7-2151-2007, 2007.

26 Alexander, J. M., and Barnet C. D.: Using satellite observations to constrain gravity wave  
27 parameterizations for global models, *J. Atmos. Sci.*, 64, 1652–1665, doi:10.1175/JAS3897.1,  
28 2007.

29 Alexander, J. M., and Teitelbaum, H.: Observation and analysis of a large amplitude  
30 mountain wave event over the Antarctic Peninsula, *J. Geophys. Res.*, 112, D21103,  
31 doi:10.1029/2006JD008368, 2007.

1 Alexander, S. P., Klekociuk, A. R., Pitts, M. C., McDonald, A. J., and Arevalo-Torres, A.:  
2 The effect of orographic gravity waves on Antarctic polar stratospheric cloud occurrence and  
3 composition, *J. Geophys. Res.*, 116, D06109, doi:10.1029/2010JD015184, 2011.

4 Alexander, S. P., Klekociuk, A. R., McDonald, A. J., and Pitts, M. C.: Quantifying the role of  
5 orographic gravity waves on polar stratospheric cloud occurrence in the Antarctic and the  
6 Arctic, *J. Geophys. Res.*, 118, 11493-11507, doi:10.1002/2013JD020122, 2013.

7 Aumann, H. H., Chahine, M. T., Gautier, C., Goldberg, M. D., Kalnay, E., McMillin, L. M.,  
8 Revercomb, H., Rosenkranz, P. W., Smith, W. L., Staelin, D. H., Strow, L. L., and Susskind,  
9 J.: AIRS/AMSU/HSB on the Aqua mission: Design, science objective, data products, and  
10 processing systems, *IEEE T. Geosci. Remote*, 41, 253–264, doi:10.1109/TGRS.2002.808356,  
11 2003.

12 Austin, J., and Butchart, N.: Coupled chemistry-climate model simulations for the period  
13 1980 to 2020: Ozone depletion and the start of ozone recovery, *Q. J. Roy. Meteor. Soc.*, 129,  
14 3225-3249, doi:10.1256/qj.02.203, 2003.

15 Austin, J., Struthers, H., Scinocca, J., Plummer, D. A., Akiyoshi, H., Baumgaertner, A. J. G.,  
16 Bekki, S., Bodeker, G. E., Braesicke, P., Brühl, C., Butchart, N., Chipperfield, M. P., Cugnet,  
17 D., Dameris, M., Dhomse, S., Frith, S., Garny, H., Gettelman, A., Hardiman, S. C., Jöckel, P.,  
18 Kinnison, D., Kubin, A., Lamarque, J. F., Langematz, U., Mancini, E., Marchand, M.,  
19 Michou, M., Morgenstern, O., Nakamura, T., Nielsen, J. E., Pitari, G., Pyle, J., Rozanov, E.,  
20 Shepherd, T. G., Shibata, K., Smale, D., Teysseèdre, H., and Yamashita, Y.: Chemistry-climate  
21 model simulations of spring Antarctic ozone, *J. Geophys. Res.*, 115, D00M11,  
22 doi:10.1029/2009JD013577, 2010.

23 Braesicke, P., Keeble, J., Yang, X., Stiller, G., Kellmann, S., Abraham, N. L., Archibald, A.,  
24 Telford, P., and Pyle, J. A.: Circulation anomalies in the Southern Hemisphere and ozone  
25 changes, *Atmos. Chem. Phys.*, 13, 10677-10688, doi:10.5194/acp-13-10677-2013, 2013.

26 Campbell, J. R., and Sassen, K.: Polar stratospheric clouds at the South Pole from 5 years of  
27 continuous lidar data: Macrophysical, optical, and thermodynamic properties, *J. Geophys.*  
28 *Res.*, 113, D20204, doi:10.1029/2007JD009680, 2008.

29 Cariolle, D., Muller, S., Cayla, F., and McCormick, M. P.: Mountain waves, polar  
30 stratospheric clouds, and ozone depletion over Antarctica, *J. Geophys. Res.*, 94, 11233-11240,  
31 doi:10.1029/JD094iD09p11233, 1989.

1 Carslaw, K. S., Wirth, M., Tsias, A., Luo, B. P., Dörnbrack, A., Leutbecher, M., Volkert, H.,  
2 Renger, W., Bacmeister, J. T., and Peter, T.: Particle microphysics and chemistry in remotely  
3 observed mountain polar stratospheric clouds, *J. Geophys. Res.*, 103, 5785-5796,  
4 doi:10.1029/97JD03626, 1998a.

5 Carslaw, K. S., Wirth, M., Tsias, A., Luo, B. P., Dörnbrack, A., Leutbecher, M., Volkert, H.,  
6 Renger, W., Bacmeister, J. T., Reimer, E., and Peter, Th.: Increased stratospheric ozone  
7 depletion due to mountain-induced atmospheric waves, *Nature*, 391, 675-678, 1998b.

8 Carslaw, K. S., Peter, T., Bacmeister, J. T., and Eckermann, S. D.: Widespread solid particle  
9 formation by mountain waves in the Arctic stratosphere, *J. Geophys. Res.*, 104, 1827-1836,  
10 doi:10.1029/1998JD100033, 1999.

11 Dean, S. M., Flowerdew, J., Lawrence, B. N., and Eckermann, S. D.: Parameterisation of  
12 orographic cloud dynamics in a GCM, *Clim. Dynam.*, 28, 581-597, doi:10.1007/s00382-006-  
13 0202-0, 2007.

14 Donlon, C. J., Martin, M., Stark, J. D., Roberts-Jones, J., Fiedler, E., and Wimmer, W.: The  
15 Operational Sea Surface Temperature and Sea Ice analysis (OSTIA), *Remote Sensing of the*  
16 *Environment*, 116, 140-158, doi:10.1016/j.rse.2010.10.017, 2011.

17 Dörnbrack, A., Leutbecher, M., Kivi, R., and Kyrö, E.: Mountain-wave-induced record low  
18 stratospheric temperatures above northern Scandinavia, *Tellus*, 51A, 951-963, 1999.

19 Dörnbrack, A., and Leutbecher, M.: Relevance of mountain waves for the formation of polar  
20 stratospheric clouds over Scandinavia: A 20 year climatology, *J. Geophys. Res.*, 106, 1583-  
21 1593, doi:10.1029/2000JD900250, 2001.

22 Dörnbrack, A., Birner, T., Fix, A., Flentje, H., Meister, A., Schmid, H., Browell, E. V., and  
23 Mahoney, M. J.: Evidence for inertia gravity waves forming in polar stratospheric clouds over  
24 Scandinavia, *J. Geophys. Res.*, 107, 8287, doi:10.1029/2001JD000452, 2002.

25 Dörnbrack, A., Pitts, M. C., Poole, L. R., Orsolini, Y. J., Nishii, K., and Nakamura, H.: The  
26 2009-2010 Arctic stratospheric winter – general evolution, mountain waves and predictability  
27 of an operational weather forecast model, *Atmos. Chem. Phys.*, 12, 3659-3675,  
28 doi:10.5194/acp-12-3659-2012, 2012.

1 Eckermann, S. D., Hoffmann, L., Höpfner, M., Wu, D. L., and Alexander, M. J.: Antarctic  
2 NAT PSC belt of June 2003: Observational validation of the mountain wave seeding  
3 hypothesis, *Geophys. Res. Lett.*, 36, L02807, doi:10.1029/2008GL036629, 2009.

4 Eyring, V., Butchart, N., Waugh, D. W., Akiyoshi, H., Austin, J., Bekki, S., Bodeker, G. E.,  
5 Boville, B. A., Brühl, C., Chipperfield, M. P., Cordero, E., Dameris, M., Deushi, M., Fioletov,  
6 V. E., Frith, S. M., Garcia, R. R., Gettelman, A., Giorgetta, M. A., Grewe, V., Jourdain, L.,  
7 Kinnison, D. E., Mancini, E., Manzini, E., Marchand, M., Marsh, D. R., Nagashima, T.,  
8 Newman, P. A., Nielsen, J. E., Pawson, S., Pitari, G., Plummer, D. A., Rozanov, E., Schraner,  
9 M., Shepherd, T. G., Shibata, K., Stolarski, R. S., Struthers, H., Tian, W., and Yoshiki, M.:  
10 Assessment of temperature, trace species and ozone in chemistry-climate model simulations  
11 of the recent past, *J. Geophys. Res.*, 111, D22308, doi:10.1029/2006JD007327, 2006.

12 Eyring, V., Arblaster, J. M., Cionni, I., Sedláček, J., Perlwitz, J., Young, P. J., Bekki, S.,  
13 Bergmann, D., Cameron-Smith, P., Collins, W. J., Faluvegi, G., Gottschaldt, K.-D., Horowitz,  
14 L. W., Kinnison, D. E., Lamarque, J.-F., Marsh, D. R., Saint-Martin, D., Shindell, D. T.,  
15 Sudo, K., Szopa, S., and Watanabe, S.: Long-term ozone changes and associated climate  
16 impacts in CMIP5 simulations, *J. Geophys. Res.*, 118, 5029-5060, doi:10.1002/jgrd.50316,  
17 2013.

18 Feng, W., Chipperfield, M. P., Davies, S., Mann, G. W., Carslaw, K. S., Dhomse, S., Harvey,  
19 L., Randall, C., and Santee, M. L.: Modelling the effect of denitrification on polar ozone  
20 depletion for Arctic winter 2004/2005, *Atmos. Chem. Phys.*, 11, 6559-6573, doi:10.5194/acp-  
21 11-6559-2011, 2011.

22 Grimsdell, A. W., Alexander, M. J., May, P. T., and Hoffmann, L.: Model study of waves  
23 generated by convection with direct validation via satellite, *J. Atmos. Sci.*, 67, 1617–1631,  
24 doi:10.1175/2009JAS3197.1, 2010.

25 Hewitt, H. T., Copsey, D., Culverwell, I. D., Harris, C. M., Hill, R. S. R., Keen, A. B.,  
26 McLaren, A. J., and Hunke, E. C.: Design and implementation of the infrastructure of  
27 HadGEM3: the next-generation Met Office climate modelling system, *Geoscientific Model  
28 Development*, 4, 223-253, doi:10.5194/gmd-4-223-2011, 2011.

29 Hoffmann, L., and Alexander, M. J.: Retrieval of stratospheric temperatures from  
30 Atmospheric Infrared Sounder radiance measurements for gravity wave studies, *J. Geophys.  
31 Res.*, 114, D07105, doi:10.1029/2008JD011241, 2009.

1 Hoffmann, L., and Alexander, M. J.: Occurrence frequency of convective gravity waves  
2 during the North American thunderstorm season, *J. Geophys. Res.*, 115, D20111,  
3 doi:10.1029/2010JD014401, 2010.

4 Hoffmann, L., Xue, X., and Alexander, M. J.: A global view of stratospheric gravity wave  
5 hotspots located with Atmospheric Infrared Sounder observations, *J. Geophys. Res.*, 118,  
6 416-434, doi:10.1029/2012JD018658, 2013.

7 Höpfner, M., Larsen, N., Spang, R., Luo, B. P., Ma, J., Svendsen, S. H., Eckermann, S. D.,  
8 Knudsen, B., Massoli, P., Cairo, F., Stiller, G., Clarmann, T. v., and Fischer, H.: MIPAS  
9 detects Antarctic stratospheric belt of NAT PSCs caused by mountain waves, *Atmos. Chem.*  
10 *Phys.*, 6, 1221-1230, doi:10.5194/acp-6-1221-2006, 2006.

11 Liu, H., Jezek, K., Li, B., Zhao, Z.: Radarsat Antarctic Mapping Project digital elevation  
12 model version 2, National Snow and Ice Data Center, Boulder, Colorado, 2001.

13 Lott, F., Miller, M.: A new subgrid scale orographic drag parameterization; its testing in the  
14 ECMWF model, *Q. J. Roy. Meteor. Soc.*, 123, 101-127, doi:10.1002/qj.49712353704, 1997.

15 Noel, V., and Pitts, M.: Gravity wave events from mesoscale simulations, compared to polar  
16 stratospheric clouds observed from spaceborne lidar over the Antarctic Peninsula, *J. Geophys.*  
17 *Res.*, 117, D11207, doi:10.1029/2011JD017318, 2012.

18 Noel, V., Hertzog, A., and Chepfer, H.: CALIPSO observations of wave-induced PSCs with  
19 near-unity optical depth over Antarctica in 2006-2007, *J. Geophys. Res.*, 114, D05202,  
20 doi:10.1029/2008JD010604, 2009.

21 McDonald, A. J., George, S. E., and Woollands, R. M.: Can gravity waves significantly  
22 impact PSC occurrence in the Antarctic?, *Atmos. Chem. Phys.*, 9, 8825-8840,  
23 doi:10.5194/acp-9-8825-2009, 2009.

24 McFarlane, N. A.: The effect of orographically excited gravity wave drag on the general  
25 circulation of the lower stratosphere and troposphere, *J. Atmos. Sci.*, 44, 1775-1800,  
26 doi:10.1175/1520-0469(1987)044<1775:TEOOEG>2.0.CO;2, 1987.

27 Morgenstern, O., Braesicke, P., O'Connor, F. M., Bushell, A. C., Johnson, C. E., Osprey, S.  
28 M., and Pyle, J. A.: Evaluation of the new UKCA climate-composition model – Part I: The  
29 stratosphere, *Geoscientific Model Development*, 2, 43-57, doi:10.5194/gmd-2-43-2009, 2009.

1 Morgenstern, O., Giorgetta, M. K., Shibata, K., Eyring, V., Waugh, D. W., Shepherd, T. G.,  
2 Akiyoshi, H., Austin, J., Baumgaertner, A. J. G., Bekki, S., Braesicke, P., Brühl, C.,  
3 Chipperfield, M. P., Cugnet, D., Dameris, M., Dhomse, S., Frith, S. M., Garny, H.,  
4 Gettelman, S., Hardiman, S. C., Hegglin, M. I., Jöckel, P., Kinnison, D. E., Lamarque, J.-F.,  
5 Mancini, E., Manzini, E., Marchand, M., Michou, M., Nakamura, T., Nielsen, J. E., Olivié,  
6 D., Pitari, G., Plummer, D. A., Rozanov, E., Scinocca, J. F., Smale, D., Teysseèdre, H.,  
7 Toohey, M., Tian W., and Yamashita, Y.: Review of the formulation of present-generation  
8 stratospheric chemistry-climate models and associated external forcings, *J. Geophys. Res.*,  
9 115, D00M02, doi:10.1029/2009JD013728, 2010.

10 Orr, A., Marshall, G., Hunt, J. C. R., Sommeria, J., Wang, C., van Lipzig, N., Cresswell, D.,  
11 and King, J. C.: Characteristics of airflow over the Antarctic Peninsula and its response to  
12 recent strengthening of westerly circumpolar winds, *J. Atmos. Sci.*, 65, 1396-1413,  
13 doi:10.1175/2007JAS2498.1, 2008.

14 Orr, A., Bechtold, P., Scinocca, J., Ern, M., and Janiskova, M.: Improved middle atmosphere  
15 climate and forecasts in the ECMWF model through a nonorographic gravity wave drag  
16 parameterization, *J. Climate*, 5905-5926, doi:10.1175/2010JCLI3490.1, 2010.

17 Orr, A., Bracegirdle T. J., Hoskings, J. S., Jung, T., Haigh, J. D., Phillips, T., and Feng, W.:  
18 Possible dynamical mechanisms for Southern Hemisphere climate change due to the ozone  
19 hole, *J. Atmos. Sci.*, 69, 2917-2932, doi:10.1175/JAS-D-11-0210.1, 2012.

20 Orr, A., Phillips, T., Webster, S., Elvidge, A., Weeks, M., Hosking, J. S., and Turner, J.: Met  
21 Office Unified Model high resolution simulations of a strong wind event in Antarctica, *Q. J.*  
22 *Roy. Meteor. Soc.*, doi:10.1002/qj.2296, 2014.

23 Pawson, S., Naujokat, B., and Labitzke, K.: On the polar stratospheric cloud formation  
24 potential of the northern stratosphere, *J. Geophys. Res.*, 100, 23215-23225,  
25 doi:10.1029/95JD01918, 1995.

26 Plougonven, R., Hertzog, A., and Teitelbaum, H.: Observations and simulations of large-  
27 amplitude mountain wave breaking over the Antarctic Peninsula, *J. Geophys. Res.*, 113,  
28 D16113, doi:10.1029/2007JD009739, 2008.

29 Plougonven, R., Arsac, A., Hertzog, A., Guez, L., and Vial, F.: Sensitivity study for  
30 mesoscale simulations of gravity waves above Antarctica during Vorcore, *Q. J. Roy. Meteor.*  
31 *Soc.*, 136, 1371-1377, doi:10.1002/qj.639, 2010.



1 Polvani, L. M., Previdi, M., and Deser, C.: Large cancellation, due to ozone recovery, of  
2 future Southern Hemisphere atmospheric circulation trends, *Geophys. Res. Lett.*, 38, L04707,  
3 doi:10.1029/2011GL046712, 2011.

4 Reinecke, P., and Durran, D. R.: The over-amplification of gravity waves in numerical  
5 solutions to flow over topography, *Mon. Weather Rev.*, 137, 1533-1549,  
6 doi:10.1175/2008MWR2630.1, 2009.

7 Roscoe, H. K., Jones, A. E., and Lee, A. M.: Midwinter start to Antarctic ozone depletion:  
8 Evidence from observations and models, *Science*, 278, 93-96,  
9 doi:10.1126/science.278.5335.93, 1997.

10 Solomon, S.: Stratospheric ozone depletion: A review of concepts and history, *Rev. Geophys.*,  
11 37, 275-316, doi:10.1029/1999RG900008, 1999.

12 Spang, R., Arndt, K., Dudhia, A., Höpfner, M., Hoffmann, L., Hurley, J., Grainger, R. G.,  
13 Griessbach, S., Poulsen, C., Remedios, J. J., Riese, M., Sembhi, H., Siddans, R., Waterfall,  
14 A., and Zehner, C.: Fast cloud parameter retrievals of MIPAS/Envisat, *Atmos. Chem. Phys.*,  
15 12, 7135–7164, doi:10.5194/acp-12-7135-2012, 2012.

16 SPARC: SPARC Report on the Lifetimes of Stratospheric Ozone-Depleting Substances, Their  
17 Replacements, and Related Species, edited by: Ko, M., Newman, P., Reimann, S., Strahan S.,  
18 SPARC Report No. 6, WCRP-15/2013, 2013.

19 Thompson, D. W. J., Solomon, S., Kushner, P. J., England, M. H., Grise, K. M., and Karoly,  
20 D. J.: Signatures of the Antarctic ozone hole in Southern Hemisphere surface climate change,  
21 *Nat. Geosci.*, 4, 741-749, 2011.

22 Webster, S., Brown, A. N., Cameron, D. R., and Jones, C. P.: Improvements to the  
23 representation of orography in the Met Office Unified Model, *Q. J. Roy. Meteor. Soc.*, 129,  
24 1989-2010, doi:10.1256/qj.02.133, 2003.

25 Webster, S., Uddstrom, M., Oliver, H., and Vosper, S.: A high-resolution modelling case  
26 study of a severe weather event over New Zealand, *Atmos. Sci. Lett.*, 9, 119-128,  
27 doi:10.1002/asl.172, 2008.

28 Wells, H., Vosper, S. B., and Yan, X.: An assessment of a mountain-wave parametrization  
29 scheme using satellite observations of stratospheric gravity waves, *Q. J. Roy. Meteor. Soc.*,  
30 137, 819-828, doi:10.1002/qj.790, 2011.

- 1 Wu, D. L.: Mesoscale gravity wave variances from AMSU-A radiances, *Geophys. Res. Lett.*,
- 2 31, L12114, doi:10.1029/2004GL019562, 2004.
- 3 Wu, D. L., and Eckermann, S. D.: Global gravity wave variances from Aura MLS:
- 4 Characteristics and interpretation, *J. Atmos. Sci.*, 65, 3695-3718,
- 5 doi:10.1175/2008JAS2489.1, 2008.
- 6

1 Table 1. Dates and times of the three mountain wave case studies for the AIRS measurements,  
 2 the start of the mesoscale and climate model simulations, and the model output time nearest  
 3 the AIRS measurements (in UTC).

Case study	AIRS measurement	Model start	Model output time nearest the AIRS measurement
CS1	7 Aug 2011, 03:40	5 Aug 2011, 12:00	7 Aug 2011, 03:00 (T + 39 h)
CS2	2 Aug 2010, 18:59	1 Aug 2010, 00:00	2 Aug 2010, 19:00 (T + 43 h)
CS3	14 Jul 2010, 20:00	13 Jul 2010, 00:00	14 Jul 2010, 20:00 (T + 44 h)

4  
 5  
 6  
 7  
 8  
 9  
 10  
 11  
 12  
 13  
 14  
 15  
 16  
 17  
 18  
 19

## 1 **Figure captions**

2 Figure 1. The temperature weighting function (brightness temperature (K) / temperature (K))  
3 for the  $666.5\text{ cm}^{-1}$  AIRS channel. This function was calculated for a polar winter reference  
4 atmosphere, a 1 km altitude grid, and the nadir observation geometry.

5

6 Figure 2. Mesoscale model (left) and climate model (right) simulation of the 850 hPa wind  
7 field ( $\text{m s}^{-1}$ ) over the Antarctic Peninsula at the time of the CS1 (**a, b**), CS2 (**c, d**), and CS3 (**e,**  
8 **f**) mountain wave events. See Table 1 for dates. The black arrows are wind vectors (for the  
9 mesoscale model only 1 in every 40 grid points is shown). The colour shading indicates the  
10 wind speed. Also shown is the coastline of the Antarctic Peninsula.

11

12 Figure 3. Measured (left) and mesoscale model (right) estimates of brightness temperature  
13 perturbations (K) corresponding to the  $666.5\text{ cm}^{-1}$  AIRS channel at the time of the CS1 (**a, b**),  
14 CS2 (**c, d**), and CS3 (**e, f**) mountain wave events. See Table 1 for dates. The horizontal black  
15 lines indicate the latitude band selected for a more detailed comparison, shown in Fig. 4. The  
16 black circles in panels b, d and f show the location of the climate model grid boxes used in  
17 Figs. 5, 7 and 8. Also shown is the coastline of the Antarctic Peninsula.

18

19 Figure 4. Measured (gray) and mesoscale model simulated (blue) brightness temperature  
20 fluctuations (K) corresponding to the  $666.5\text{ cm}^{-1}$  AIRS channel along a latitude band  
21 intersecting the Antarctic Peninsula (indicated on Fig. 3) at the time of the CS1 (**a**), CS2 (**b**),  
22 and CS3 (**c**) mountain wave events. See Table 1 for dates. Model data have been re-sampled  
23 on the AIRS measurement grid. Note that the model domain does not always cover the full  
24 AIRS swath, therefore re-gridded model data are missing at some longitudes in CS1 and CS2.  
25 The solid lines show a  $1^\circ$  running mean in longitude of the individual temperature  
26 fluctuations.

27

28 Figure 5. Vertical profile of temperature fluctuations (K) resolved by the climate model  
29 (dashed line), resolved by the mesoscale model (stars and horizontal bars), and parameterised  
30 by the mountain wave scheme  $\Delta T_{SSO}$  (solid line) at the time of the CS1 (**a**), CS2 (**b**), and CS3

1 (c) mountain wave events. See Table 1 for dates. The temperature fluctuations resolved by  
2 the climate model and parameterised by the scheme are for the grid boxes located at (70°S,  
3 63.75°W) for CS1, (65.0°S, 60.0°W) for CS2, and (70.0°S, 60°W) for CS3, i.e. selected to  
4 coincide with the location of their respective mountain wave events. These locations are  
5 displayed on Fig. 3. The mesoscale model temperature fluctuations are the mean (stars) and  
6 spread ( $\pm$  two standard deviations, horizontal bars) of all the mesoscale model points within  
7 the same climate model grid box.

8

9 Figure 6. Vertical cross section intersecting the Antarctic Peninsula along a latitude band at  
10 70°S of the temperature fluctuations (K) simulated by the mesoscale model (a) and  
11 parameterised by the mountain wave scheme (b) at the time of the CS3 mountain wave event.  
12 See Table 1 for dates. The grey shading indicates the height of the explicitly resolved  
13 orography. Also shown is the cooling phase of the parameterised temperature fluctuations  
14  $\Delta T_{SSO}^-$  (c), i.e. the field which is actually coupled to the PSC scheme of the chemistry-climate  
15 model.

16

17 Figure 7. Vertical profile of the wind speed  $U$  (resolved in the direction of the wave vector,  
18 which is taken to be the direction of the 850 hPa wind vector) simulated by the climate model  
19 (black line) and the mesoscale model (grey lines) at the time of the CS1 (a), CS2 (b), and CS3  
20 (c) mountain wave events. See Table 1 for dates. The climate model profile is for the same  
21 grid box used for Fig. 5. The mesoscale model profiles are for all the mesoscale model points  
22 within the same climate model grid box.

23

24 Figure 8. As Fig. 6, but for Brunt-Väisälä frequency  $N$  ( $s^{-1}$ ).

25

26 Figure 9. Impact of the mountain wave parameterisation during July at 21 km on the  
27 frequency  $f$  the 195 K (a) and 188 K (b) temperature thresholds are exceeded over the  
28 Antarctic Peninsula in the perturbation run of the chemistry-climate model. Shown are the  
29 30-year average percentage point difference between the frequency based on the explicitly  
30 resolved temperature  $T_{CHEM-CLIM}$  plus the parameterised temperature fluctuations  $\Delta T_{SSO}^-$ , and

1 the frequency based solely on  $T_{CHEM-CLIM}$ , i.e.  $f_{T_{CHEM-CLIM} + \Delta T_{SSO}^-} - f_{T_{CHEM-CLIM}}$ . In the perturbed  
2 run,  $\Delta T_{SSO}$  is represented by the cooling phase  $\Delta T_{SSO}^-$  only. The temperature thresholds of 195  
3 and 188 K are assumed to be representative of the formation of type I and II PSCs,  
4 respectively. Both differences are computed from 6 hourly fields. The contours indicate the  
5 30-year average frequency  $f_{T_{CHEM-CLIM}}$ . Also shown is the coastline of the Antarctic Peninsula.

6

7 Figure 10: Impact of the mountain wave parameterisation during July at 21 km on the  
8 probability distributions of temperature over the Antarctic Peninsula in the perturbed run of  
9 the chemistry-climate model. Shown are the 30-year average temperature distributions based  
10 on the explicitly resolved temperature  $T_{CHEM-CLIM}$  plus the parameterised temperature  
11 fluctuations  $\Delta T_{SSO}^-$  (red colouring), and the frequency based solely on  $T_{CHEM-CLIM}$  (gray  
12 colouring). Regions where the two distributions overlap is coloured the darker shade of red.  
13 Both temperature distributions are for the N48 grid box as used in Figs. 5, 7 and 8. In the  
14 perturbed run,  $\Delta T_{SSO}$  is represented by the cooling phase  $\Delta T_{SSO}^-$  only. The temperature  
15 thresholds of 195 and 188 K are marked as dashed vertical lines and are assumed to be  
16 representative of the formation of type I and II PSCs, respectively. Both temperature  
17 distributions are computed from 6 hourly fields.

18

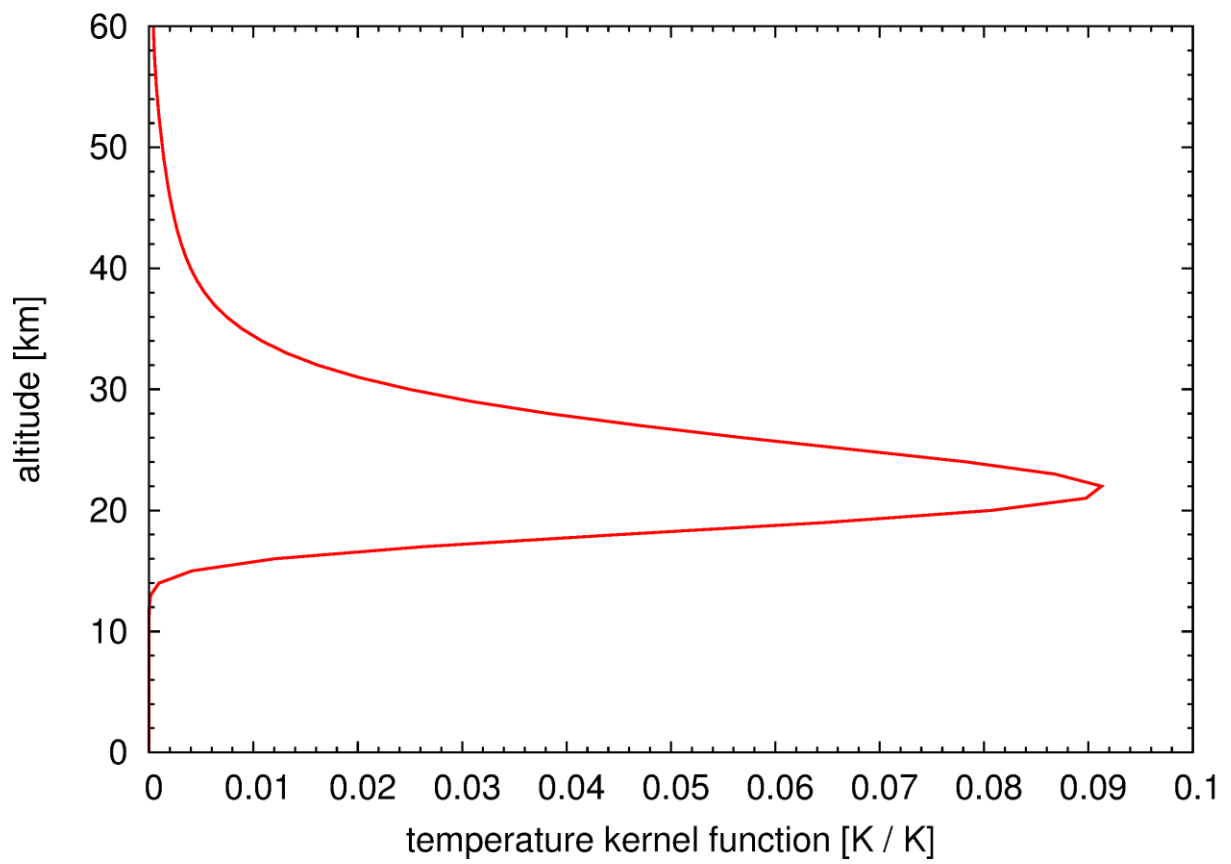
19 Figure 11. Impact of the mountain wave parameterisation during July at 21 km on PSC  
20 surface area density ( $\mu\text{m}^2 \text{cm}^{-3}$ ) over the Antarctic Peninsula in the chemistry-climate model.  
21 The shading indicates the 30-year average difference in surface area density between the  
22 perturbation run and the control run (perturbation run minus the control run) for PSC types I  
23 and II **(a)**, type I **(b)**, and type II **(c)**. The contours indicate the 30-year average PSC surface  
24 area density from the control run. Hatching denotes significance at the 95% confidence level  
25 using a two-tailed Student's T-Test. Also shown is the coastline of the Antarctic Peninsula.

26

27

28

29

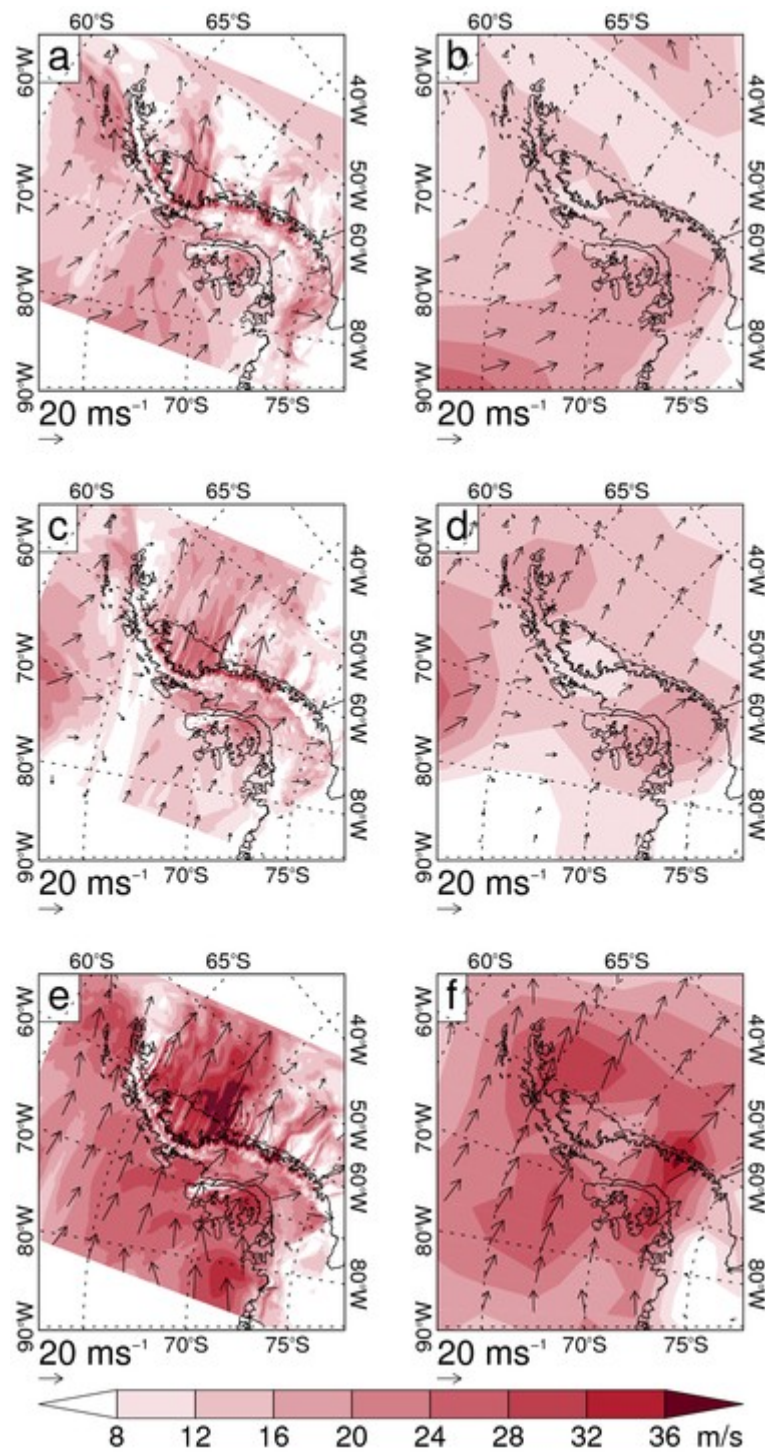


1

2

3 Figure 1. The temperature weighting function (brightness temperature (K) / temperature (K))  
4 for the  $666.5 \text{ cm}^{-1}$  AIRS channel. This function was calculated for a polar winter reference  
5 atmosphere, a 1 km altitude grid, and the nadir observation geometry.

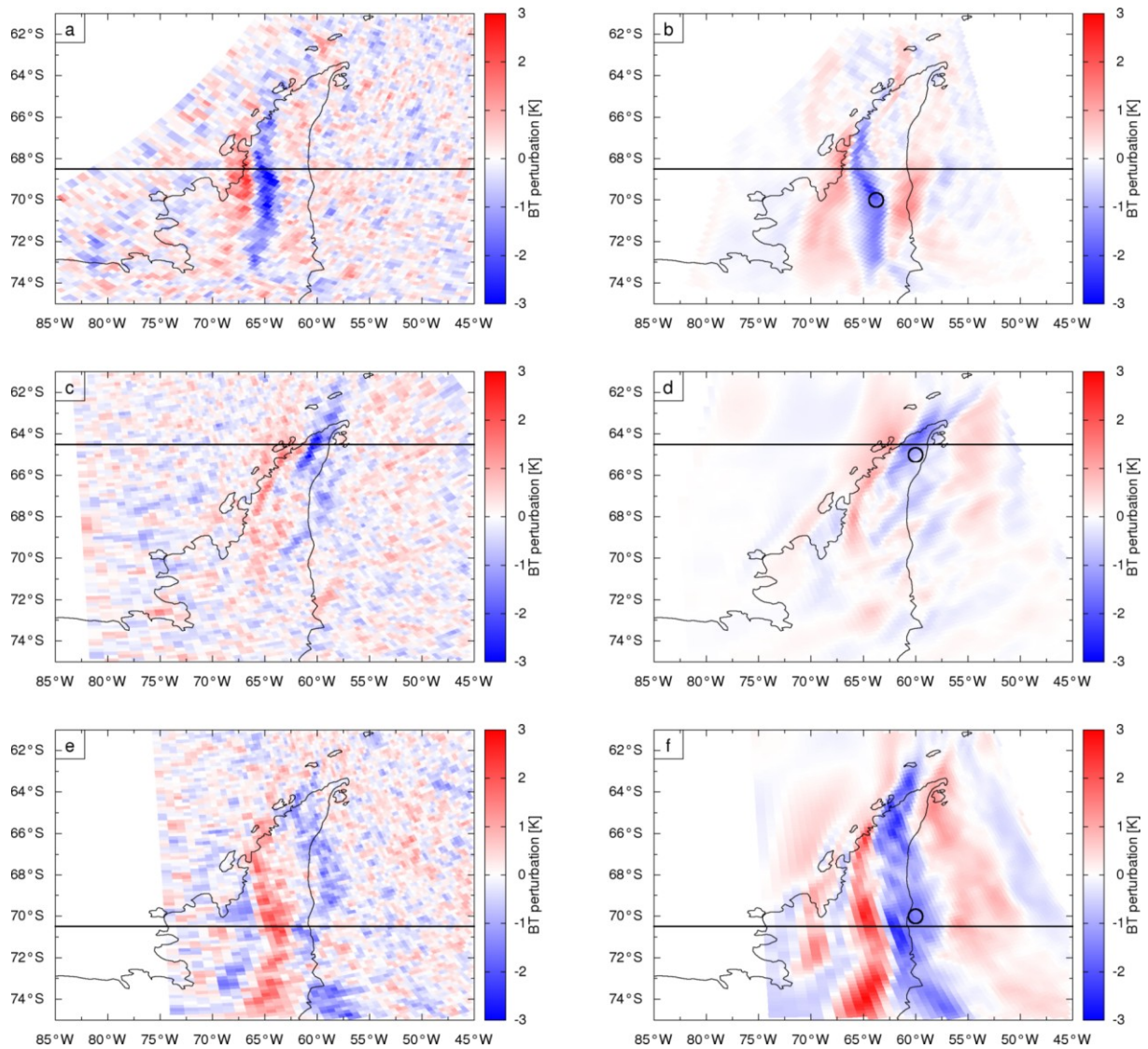
6



1  
2

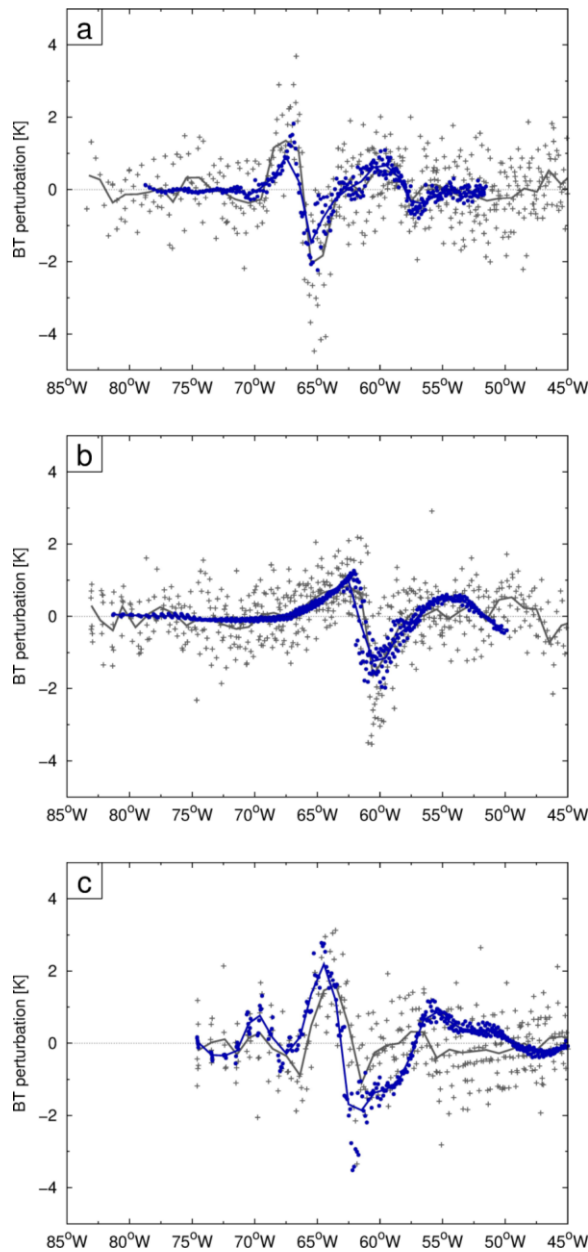
3 Figure 2. Mesoscale model (left) and climate model (right) simulation of the 850 hPa wind  
 4 field ( $\text{m s}^{-1}$ ) over the Antarctic Peninsula at the time of the CS1 (a, b), CS2 (c, d), and  
 5 CS3 (e, f) mountain wave events. See Table 1 for dates. The black arrows are wind vectors (for the  
 6 mesoscale model only 1 in every 40 grid points is shown). The colour shading indicates the  
 7 wind speed. Also shown is the coastline of the Antarctic Peninsula.





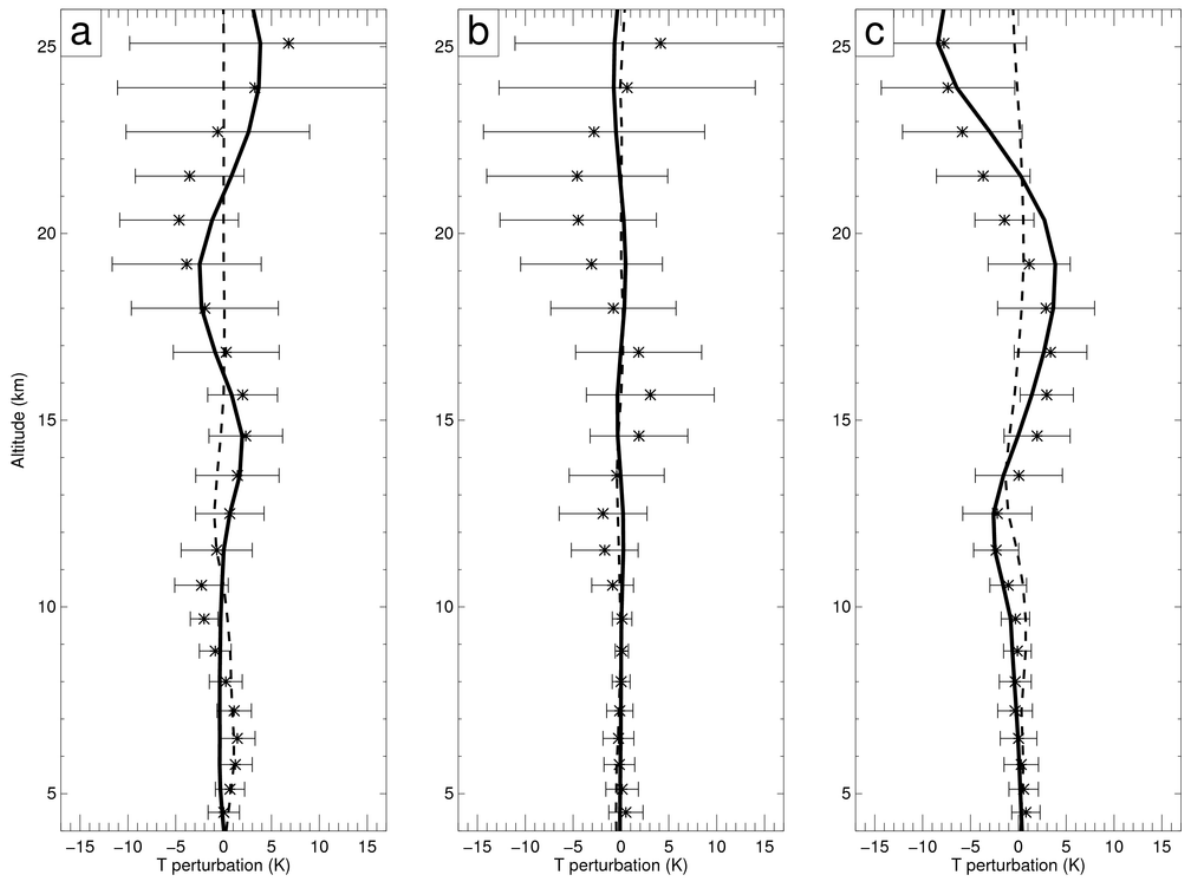
1  
2  
3  
4  
5  
6  
7  
8  
9

Figure 3. Measured (left) and mesoscale model (right) estimates of brightness temperature perturbations (K) corresponding to the  $666.5\text{ cm}^{-1}$  AIRS channel at the time of the CS1 (**a, b**), CS2 (**c, d**), and CS3 (**e, f**) mountain wave events. See Table 1 for dates. The horizontal black lines indicate the latitude band selected for a more detailed comparison, shown in Fig. 4. The black circles in panels b, d and f show the location of the climate model grid boxes used in Figs. 5, 7 and 8. Also shown is the coastline of the Antarctic Peninsula.



1  
2  
3  
4  
5  
6  
7  
8  
9  
10

Figure 4. Measured (gray) and mesoscale model simulated (blue) brightness temperature fluctuations (K) corresponding to the  $666.5 \text{ cm}^{-1}$  AIRS channel along a latitude band intersecting the Antarctic Peninsula (indicated on Fig. 3) at the time of the CS1 (a), CS2 (b), and CS3 (c) mountain wave events. See Table 1 for dates. Model data have been re-sampled on the AIRS measurement grid. Note that the model domain does not always cover the full AIRS swath, therefore re-gridded model data are missing at some longitudes in CS1 and CS2. The solid lines show a  $1^\circ$  running mean in longitude of the individual temperature fluctuations.



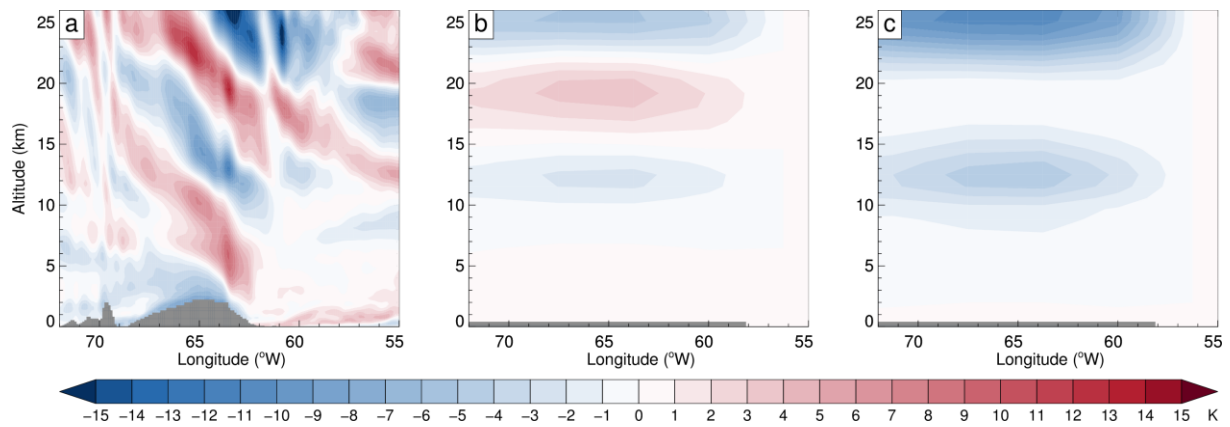
1

2 Figure 5. Vertical profile of temperature fluctuations (K) resolved by the climate model  
 3 (dashed line), resolved by the mesoscale model (stars and horizontal bars), and parameterised  
 4 by the mountain wave scheme  $\Delta T_{SSO}$  (solid line) at the time of the CS1 (a), CS2 (b), and CS3  
 5 (c) mountain wave events. See Table 1 for dates. The temperature fluctuations resolved by  
 6 the climate model and parameterised by the scheme are for the grid boxes located at (70°S,  
 7 63.75°W) for CS1, (65.0°S, 60.0°W) for CS2, and (70.0°S, 60°W) for CS3, i.e. selected to  
 8 coincide with the location of their respective mountain wave events. These locations are  
 9 displayed on Fig. 3. The mesoscale model temperature fluctuations are the mean (stars) and  
 10 spread ( $\pm$  two standard deviations, horizontal bars) of all the mesoscale model points within  
 11 the same climate model grid box.

12

13

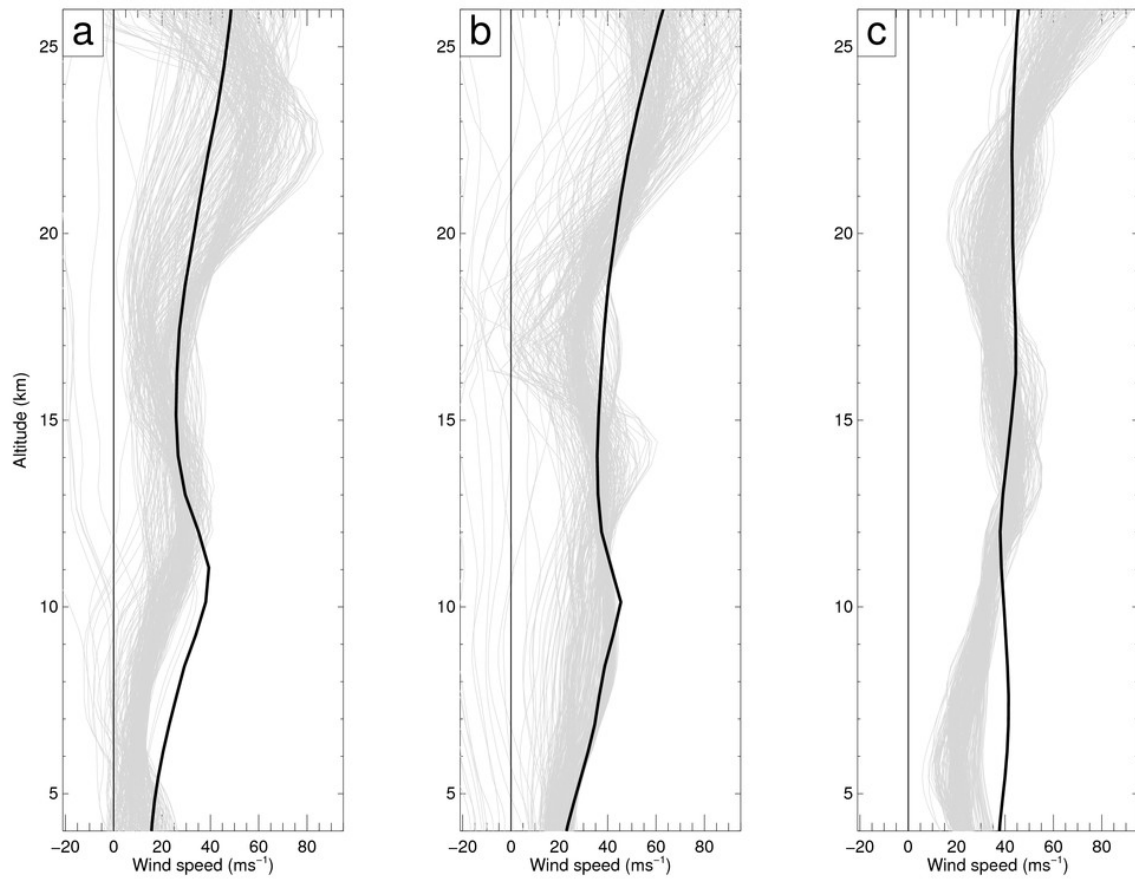
14



1  
2

3 Figure 6. Vertical cross section intersecting the Antarctic Peninsula along a latitude band at  
 4 70°S of the temperature fluctuations (K) simulated by the mesoscale model **(a)** and  
 5 parameterised by the mountain wave scheme **(b)** at the time of the CS3 mountain wave event.  
 6 See Table 1 for dates. The grey shading indicates the height of the explicitly resolved  
 7 orography. Also shown is the cooling phase of the parameterised temperature fluctuations  
 8  $\Delta T_{SSO}^-$  **(c)**, i.e. the field which is actually coupled to the PSC scheme of the chemistry-climate  
 9 model.

10  
11  
12  
13  
14  
15  
16



1

2

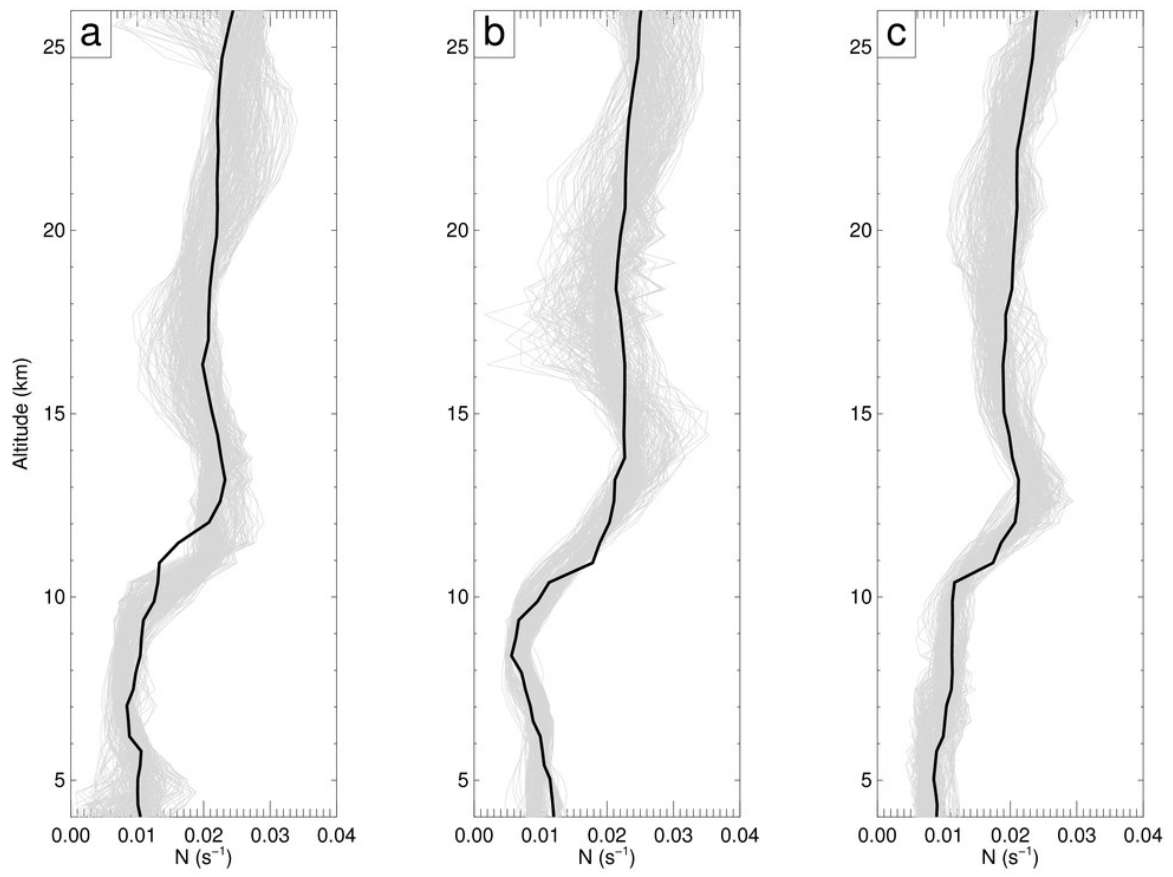
3 Figure 7. Vertical profile of the wind speed  $U$  (resolved in the direction of the wave vector,  
 4 which is taken to be the direction of the 850 hPa wind vector) simulated by the climate model  
 5 (black line) and the mesoscale model (grey lines) at the time of the CS1 (a), CS2 (b), and CS3  
 6 (c) mountain wave events. See Table 1 for dates. The climate model profile is for the same  
 7 grid box used for Fig. 5. The mesoscale model profiles are for all the mesoscale model points  
 8 within the same climate model grid box.

9

10

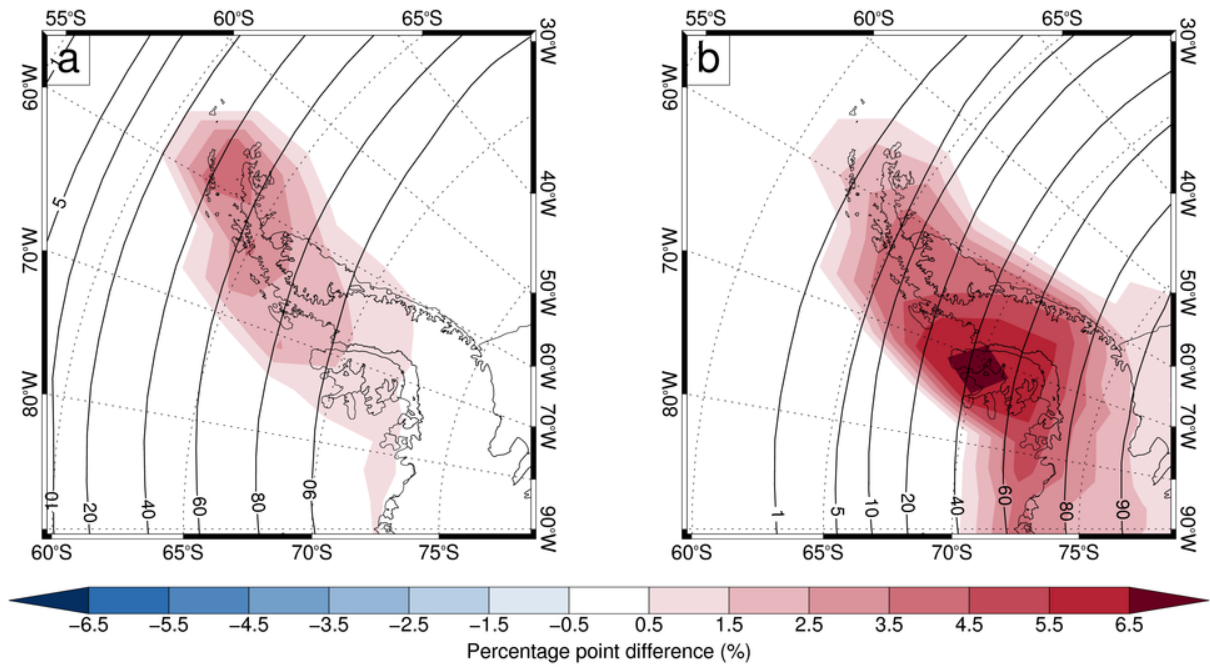
11

12



1  
2  
3  
4  
5  
6  
7

Figure 8. As Fig. 6, but for Brunt-Väisälä frequency  $N$  ( $s^{-1}$ ).



1

2

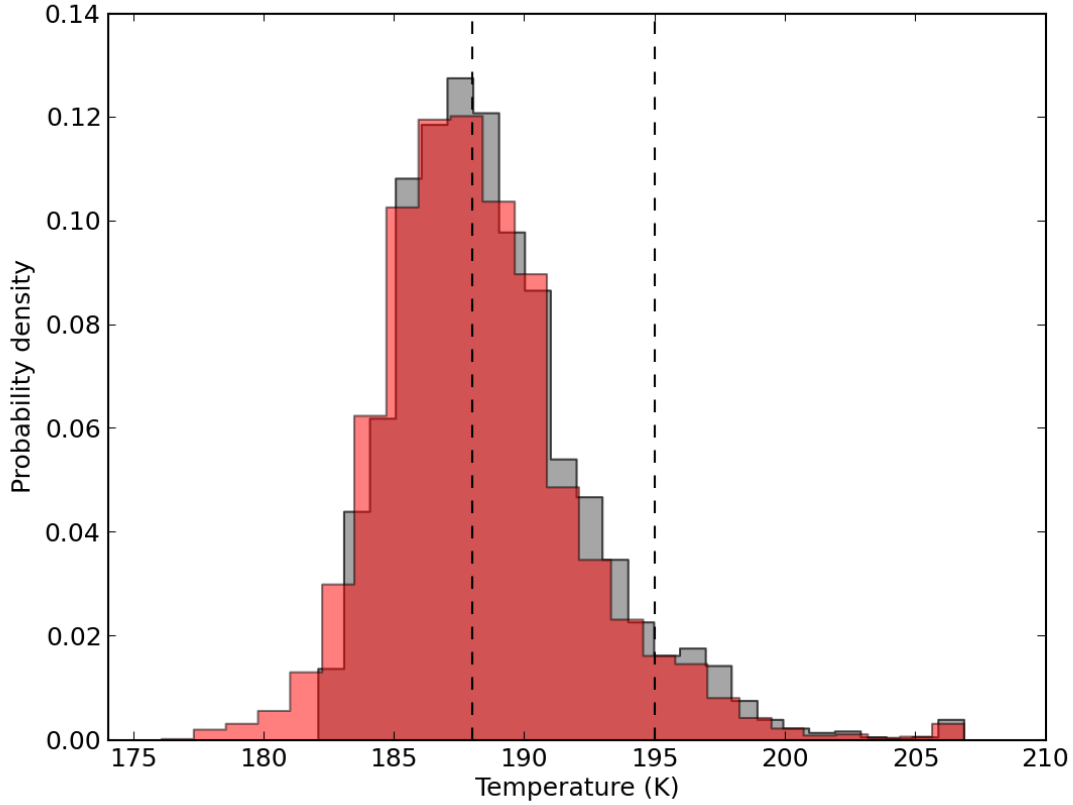
3 Figure 9. Impact of the mountain wave parameterisation during July at 21 km on the  
 4 frequency  $f$  the 195 K **(a)** and 188 K **(b)** temperature thresholds are exceeded over the  
 5 Antarctic Peninsula in the perturbation run of the chemistry-climate model. Shown are the  
 6 30-year average percentage point difference between the frequency based on the explicitly  
 7 resolved temperature  $T_{CHEM-CLIM}$  plus the parameterised temperature fluctuations  $\Delta T_{SSO}^-$ , and  
 8 the frequency based solely on  $T_{CHEM-CLIM}$ , i.e.  $f_{T_{CHEM-CLIM} + \Delta T_{SSO}^-} - f_{T_{CHEM-CLIM}}$ . In the perturbed  
 9 run,  $\Delta T_{SSO}$  is represented by the cooling phase  $\Delta T_{SSO}^-$  only. The temperature thresholds of 195  
 10 and 188 K are assumed to be representative of the formation of type I and II PSCs,  
 11 respectively. Both differences are computed from 6 hourly fields. The contours indicate the  
 12 30-year average frequency  $f_{T_{CHEM-CLIM}}$ . Also shown is the coastline of the Antarctic Peninsula.

13

14

15

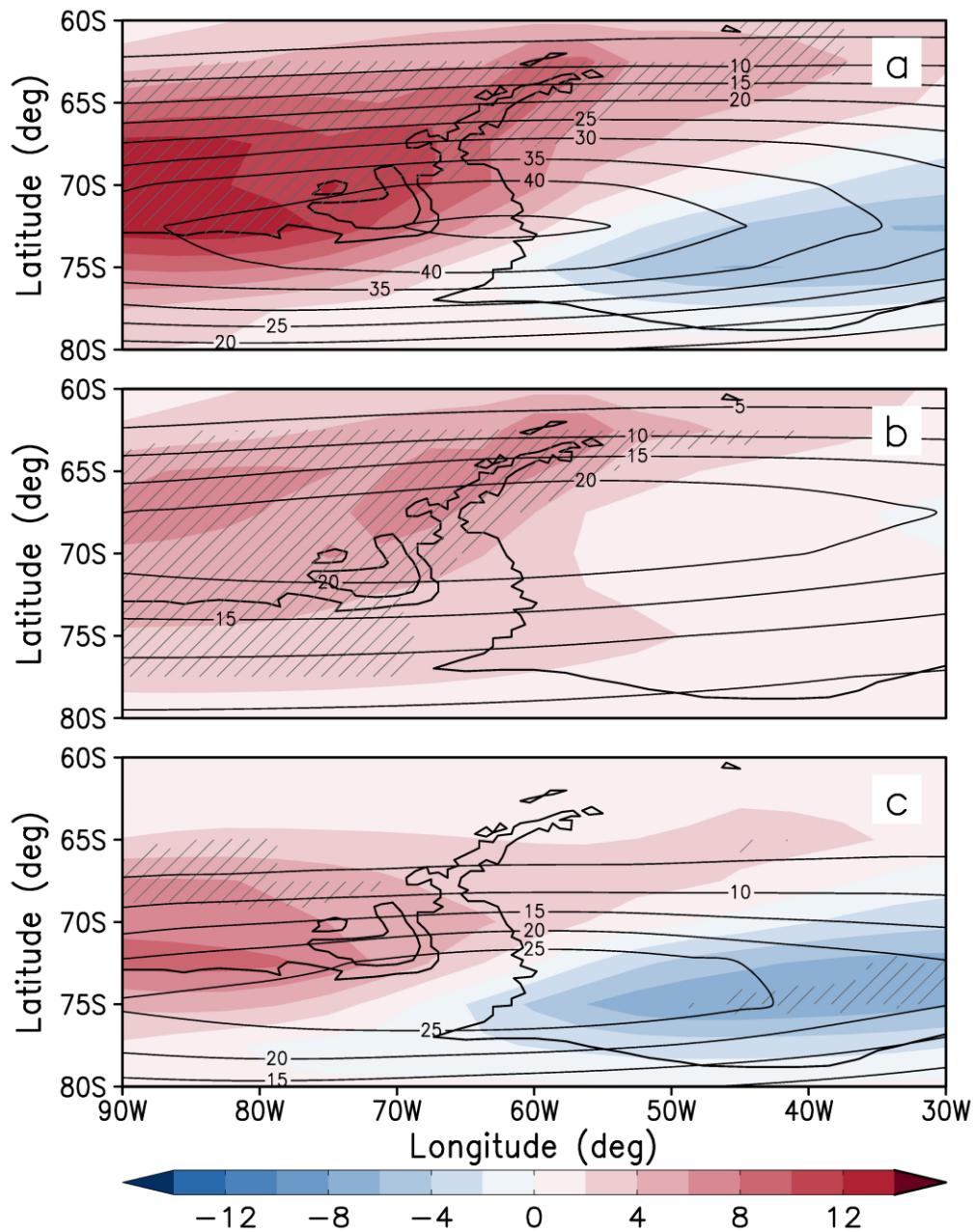
16



1  
2 Figure 10: Impact of the mountain wave parameterisation during July at 21 km on the  
3 probability distributions of temperature over the Antarctic Peninsula in the perturbed run of  
4 the chemistry-climate model. Shown are the 30-year average temperature distributions based  
5 on the explicitly resolved temperature  $T_{CHEM-CLIM}$  plus the parameterised temperature  
6 fluctuations  $\Delta T_{SSO}^-$  (red colouring), and the frequency based solely on  $T_{CHEM-CLIM}$  (gray  
7 colouring). Regions where the two distributions overlap is coloured the darker shade of red.  
8 Both temperature distributions are for the N48 grid box as used in Figs. 5, 7 and 8. In the  
9 perturbed run,  $\Delta T_{SSO}^-$  is represented by the cooling phase  $\Delta T_{SSO}^-$  only. The temperature  
10 thresholds of 195 and 188 K are marked as dashed vertical lines and are assumed to be  
11 representative of the formation of type I and II PSCs, respectively. Both temperature  
12 distributions are computed from 6 hourly fields.

13





1

2

3 Figure 11. Impact of the mountain wave parameterisation during July at 21 km on PSC  
 4 surface area density ( $\mu\text{m}^2 \text{cm}^{-3}$ ) over the Antarctic Peninsula in the chemistry-climate model.  
 5 The shading indicates the 30-year average difference in surface area density between the  
 6 perturbation run and the control run (perturbation run minus the control run) for PSC types I  
 7 and II **(a)**, type I **(b)**, and type II **(c)**. The contours indicate the 30-year average PSC surface  
 8 area density from the control run. Hatching denotes significance at the 95% confidence level  
 9 using a two-tailed Student's T-Test. Also shown is the coastline of the Antarctic Peninsula.

10